Seismic High-Resolution Acquisition Electronics for the NASA InSight Mission on Mars

Peter Zweifel, Davor Mance, Jan ten Pierick, Domenico Giardini, Cedric Schmelzbach, Thomas Haag, Tobias Nicollier, Savas Ceylan, Simon Stähler, Martin van Driel, et al.

Seismic High-Resolution Acquisition Electronics for the NASA InSight Mission on Mars

P. Zweifel[1,*], D. Mance[1], J. ten Pierick[1], D. Giardini[1], C. Schmelzbach[1], T. Haag[1], T. Nicollier[6], S. Ceylan[1], S. Stähler[1], M. van Driel[1], D. Sollberger[1], F. Euchner[1], J.F. Clinton[1], M. Bierwirth[2], M. Eberhardt[2], P.Lognonné[3], W.T. Pike[4], W.B. Banerdt[5]

[*] Corresponding author: Peter Zweifel, Institute of Geophysics, ETH Zurich, c/o Schachenstrasse 39a, 8633 Wolfhausen, Switzerland, +41 79 572 85 82, peter.zweifel@retired.ethz.ch

[1] Eidgenössische Technische Hochschule Zürich

[2] Max-Planck-Institute for Solar System Research, Göttingen

[3] Institut de Physique du Globe de Paris

[4] Imperial College London

[5] Jet Propulsion Laboratory / California Institute of Technology

[6] Eidgenössische Forschungsanstalt WSL, Birmensdorf

Declaration of Competing Interests

The authors acknowledge there are no conflicts of interest recorded.

Abstract

The InSight (Interior exploration using Seismic Investigations, Geodesy and Heat Transport) seismometer instrument SEIS (Seismic Experiment for Interior Structure) was deployed on Mars in December 2018 and went into scientific operation mode starting from March 2019. The

Acquisition and Control electronics (AC) is a key element of SEIS. The AC acquires the seismic signals of the two sets of seismic sensors with high resolution, stores the data in its local non-volatile memory for later transmission by the lander and controls the numerous functions of SEIS. In this paper, we present an overview of the AC with its connections to the sensors and to the lander, as well as its functionality. We describe the elements of the acquisition chains and filters, and discuss the performance of the seismic and temperature channels. Furthermore, we outline the safety functions and health monitoring, which are of paramount importance for reliable operation on Mars. In addition, we analyze an artefact affecting the seismic data referred to as the 'tick-noise', and provide a method to remove this artefact by post-processing the data.

Introduction

NASA InSight landed on Mars on November 26, 2018 (Banerdt et al., 2020). The InSight lander is equipped with three instruments:

- SEIS: consisting of a very broadband (VBB) and one short period (SP) seismometer each with three components (P. Lognonné, 2019)
- HP^3: Heat Flow and Physical Properties Package (Spohn et al., 2018)
- RISE: Rotation and Interior Structure Experiment (Folkner et al., 2018)

SEIS is the primary instrument of the mission. Between December 2018 and March 2019, after initial operation of the lander, SEIS was commissioned, configured and deployed on the surface of Mars, and then began scientific operation.

SEIS consists of three main parts:

- the Sensor Assembly (SA), which was placed on the ground by the InSight's robotic arm
- the Electronics Box (E-Box), which resides in the temperature-controlled lander compartment, called the Warm Electronics Box (WEB)

- the tether connecting the SA to the E-Box

The SA incorporates the seismic sensors, the leveling mechanism and a thermal protection (Figure 1). Three identical, oblique-oriented VBB sensor axes are located in a vacuum sphere and mounted on the ring-shaped leveling structure (LVL). Each VBB sensor has a proximity electronics attached to the LVL. One vertical and two horizontal SP sensors are fixed on the outer side of LVL separated at angles of 120 degrees. The LVL has three extendable legs, which can be adjusted in order to level the SA on a slope of up to 15 degrees. (A detailed description of the SEIS instrument can be found in (P. Lognonné, 2019)).

There are temperature sensors installed on each of the VBB and SP sensors, in the VBB proximity electronics and on the structure. The latter is used to measure the SA temperature with high resolution for decorrelation purposes. Each VBB sensor includes a motor driven mass centering and a temperature compensation mechanism. The LVL is equipped with motors to move the legs, supported by coarse and high-precision tilt-meters. Heaters are attached to the inner side of the LVL ring to keep the SA temperature above -65 ºC and thus within the safe operating temperature range. A double-walled thermal enclosure (RWEB) covers and protects the entire SA. After deployment on ground, a Wind and Thermal Shield (WTS) is placed over the SA to complete the protection and insulation of the sensitive sensors.

The tether is the electrical connection between the SA and the E-Box. It is a 3 m long semi-rigid, layered flat cable (partially visible in Figure 1) carrying about 200 wires for the sensor signals, power and ground connections, control signals, measurement signals, motor drive lines for leveling, mass-centering, etc.

Here, we give a brief description of the SEIS electronics. We then describe the seismic data acquisition channels and processing chain. We present the acquisition performance of the seismic and the temperature channels. Finally, we describe an artefact caused by the electronics,

which we refer to as the “tick noise”, and provide a method of removing it from the seismic dataset.

SEIS Electronics

The E-Box comprises all SEIS electronics, except the VBB proximity electronics, some electronics inside the SP sensors and the high precision tiltmeter front end electronics mounted on the LVL. The E-Box is located in a triangle-shaped space in the WEB, hanging upside down below the lander deck. The WEB contains most of the lander and instrument electronics and is heated to prevent temperatures to fall below -35 ºC. The picture in Figure 2 shows the E-Box Flight Model (FM) unit in preparation for the thermal test.

The E-Box is implemented as a modular structure and includes all SEIS boards (see exploded view in Figure 2):

- Power distribution and conditioning electronics (DC), two boards
- Acquisition electronics (ACQ), one board
- Control electronics (CTL), two boards
- VBB Feedback electronics VBB-FB[123], three boards
- SP Feedback electronics SP-FB, one board for all three axes
- Leveling Motor Drive Electronics LVL-MDE, one board

The Acquisition and Control electronics (AC) consists of the ACQ, CTL and DC boards. It constitutes a sophisticated seismic data logger that provides, besides the high-resolution acquisition of seismic sensors, the power for the instrument and a variety of functions to run the instrument fully remote controlled in the environment of Mars as described later in this paper. It is the core of the SEIS instrument and provides interfaces to the Command & Data Handling Unit (C&DH) and Power Distribution & Drive Unit (PDDU) on the lander side, and to the instrument’s sub-systems (VBB and SP sensors, LVL).

Since SEIS is the primary instrument of the InSight mission, reliability is paramount. The instrument has to withstand "single-point failures". This is accomplished by duplicating vital parts of the instrument. The two sensor packages (VBB and SP) with their associated electronics meet this requirement, since an SP sensor can replace a defective VBB sensor to a certain extent and vice versa. Their associated electronics consist of the sensor feedback electronics and the acquisition front-end circuits of the AC, with the latter providing signal conditioning and the analog-to-digital conversion.

The AC, which is the central part of the instrument, is duplicated except for the aforementioned front-end circuitry and the LVL-MDE electronics. This means that there are two identical electronics, called the A-side and B-side of the AC. In the event of a fault, the B-side can substitute the defective A-side or vice versa. The A-side is used for nominal operation. The sensor and associated electronics as well as the LVL-MDE are connected to both sides of the AC. The PDDU supplies the SEIS instrument with four +28 V primary power lines. Two of these lines are connected to the A-side and two to the B-side of the AC. The C&DH (likewise duplicated) controls the PDDU switches so that one of the four power lines is powered-up, activating the corresponding A or B side of the AC.

The LVL MDE board is not duplicated due to volume and mass constraints in the WEB and limitations on the number of wires in the cable. The associated risk is considered acceptable because sensor leveling is rarely used and is only activated when temperatures are highest on Mars.

As a further safety measure, each sensor-axis can be switched off individually to isolate defective sensors or circuits. Automatic over-current protection circuits switch off parts or all of the electronics. To detect potential problems or adverse trends, numerous housekeeping channels measure currents, voltages and temperatures in the various instrument parts. The housekeeping

data is stored and downlinked to Earth for health monitoring by the instrument operation engineers.

The block diagram in Figure 2 shows the main connections within the SEIS instruments to the spacecraft and to the Auxiliary Payload Sensor Suite (APSS) (see Banfield, 2018). The DC boards convert the primary power into several positive and negative supply voltages required by the AC and the sub-systems. The duplicated interfaces to the lander computers C&DH A and C&DH B are cross-strapped and consist of a low speed serial line for commands and special data, and a serial 4 Mbit/s line for the high-speed transmission of acquired sensor and health data to the lander for further processing or downlink to Earth.

The SEIS command dictionary incorporates eighty commands with various parameters to cover all functions of the SEIS instrument, such as turning on sub-systems, starting/stopping the acquisition, configuring sampling rates and gains, retrieving specific data, and so on. The APSS receives a 1-second pulse from SEIS. This pulse is used to time-correlate the APSS data with SEIS data.

Seismic Acquisition Channels

There are nine seismic acquisition channels. The VBB sensors provide three velocity and three position signals, the SP sensors three velocity signals. Each of these signals is digitized by a dedicated 24-bit sigma-delta Analog-to-Digital Converter (ADC) and then filtered, time-stamped and stored in the on-board non-volatile memory. The lander computer C&DH retrieves the data regularly and then processes and stores the data in its mass memory. The acquired and processed data can then be downlinked to Earth on request.

Acquisition Chain

The acquisition chain consists of the conditioning electronics (amplifier/filter), the ADC and the Finite Impulse Filter (FIR; see block diagram in Figure 3). The conditioning electronics in front of the ADC scales the seismic signals from the sensor full-scale range to the input voltage range of the ADC. The full-scale ranges are ±25 Volt for the VBBs (for both velocity and position signals) and ±12.5 Volt for the SP velocity signals. In addition, the conditioning electronics filters the signal by the second-order low pass filter, which is the first part of a 3-step anti-aliasing filter. To reduce the low frequency (1/f) noise, low offset, zero drift (auto zero) amplifiers are used.

Analog-to-Digital Conversion

The performance requirement "seismic signals with a dynamic range of at least 130 dB in amplitude" require the use of a 24-bit ADC. At the time the InSight development began in 2012, 24-bit ADC's were state-of-the-art in seismic data loggers and in industry in general, but not common in space projects. The challenge for these rather complex integrated circuits is to sustain the impact of cosmic radiation in space when departing the protective magnetosphere of Earth, and after landing on Mars. The 24-bit sigma-delta ADC AD7712 was finally selected for SEIS due to its robustness with respect to radiation and its availability in MIL quality (military temperature range and ceramic packaging). The device passed the radiation tests without any permanent destruction although it showed some malfunctions that altered configuration registers and interrupted the conversion. These failure conditions are managed in operation by monitoring and rewriting the ADC's configuration registers.

The ADC converts the signals with an input sampling rate of 32 kHz. The on-chip 3rd order sinc-in-time filter (sinc^3) is followed by a decimation by a factor of 64 for the velocity channels and by a factor of 3200 for the position channels. The corresponding ADC output rates are thus

500 Hz for VBB and SP velocity and 10 Hz for VBB position. This $sinc^3$ filter constitutes the second stage of the anti-aliasing filtering.

FIR Filter

The FIR filters, implemented in the Field Programmable Gate Array (FPGA), apply a sharp low-pass filter, which allows decimating the filter output data to the final output rates. For the VBB and SP velocity channels, a sampling rate of 100 Hz or 20 Hz is selectable. The upper diagram in Figure 4 shows the corresponding filter layout. If 100 Hz data is selected, only stage 1 is used, i.e., the output samples of stage 1 will end up in the data packet. If 20 Hz data is selected, both stages are used and the output samples of stage 2 will end up in the data packet.

For the VBB position and Scientific Temperature SCIT (LVL temperature) channels, the sampling rates of 1 Hz and 0.1 Hz are available. The corresponding filter layout is shown in the lower diagram in Figure 4.

The FIR filter is the third and last stage of the anti-aliasing filtering. The standard filter used for seismic recordings is identical to the terrestrial broadband seismological station CI.PFO (refer to P. Lognonné, 2019).

The data samples of the seismic and the temperature channels are buffered and then 1-second data packets are constructed from them. These packets are time-stamped with the Local On-Board Time (LOBT) that corresponds to the instant when the first sample of the 1-second data packet was acquired. The packets are stored in the FLASH memory, which can hold more than 65 hours of data. The FLASH memory is organized as a ring buffer; i.e., as soon as the memory is filled-up, the oldest data is overwritten.

Anti-aliasing Filter

The resulting anti-aliasing filter is the product of the three filter steps mentioned in the previous sections. The first two steps are implemented as hardware, only the FIR filter in FPGA can be

configured. Figure 3 left side shows the individual attenuation of each of the three filter steps up to 600 Hz.

It can be seen that the FPGA filters do not suppress signals with a frequency of 500 Hz ± 8 Hz, as these signals appear in the pass band due to folding around the ADC Nyquist frequency of 250 Hz. However, this effect coincides with the notch of the ADC filters at 500 Hz. Therefore, the total attenuation of the cascaded filters remains at almost 120 dB for frequencies above the pass band (see Figure 3 right hand side). The contribution of the analog filter (first filter step) is less than 10 dB in the frequency range shown.

FIR Filter upload

The FIR filter coefficients can be uploaded from Earth via the lander and changed for certain channel groups. Channel groups are VBB velocity channels, SP velocity channels, VBB position channels and the SCIT channel. This capability is used to change filters for special purposes, as for example, to achieve an extended bandwidth as described in the section ‘Strategies to record information beyond the Nyquist frequency of 50 Hz’.

Channel Noise Performance

The acquisition noise is a result of the amplifier noise of the signal conditioning, the intrinsic noise of the ADC and the voltage reference noise (Figure 5). The ADC intrinsic noise of 3.8 $\mu V/\sqrt{Hz}$ is flat (white) down to 10 mHz, below which the ADC 1/f noise becomes visible. Above about 8 Hz, the ADC quantization noise starts to dominate over the ADC white noise and becomes therefore visible at 100 Hz data rate up to the FIR filter corner frequency of 40 Hz.

A space qualified external voltage reference (RH1021-5), with a temperature sensitivity of <5 ppm/K is used to achieve good stability. It has a low noise, matching the ADC performance.

The acquisition noise level at low frequencies (<100 mHz) depends on the input signal amplitude since the voltage reference noise is proportionally scaled with the acquired signal. For signals

less than about 25% of the full-scale range (FSR), the voltage reference noise is not significant w.r.t. the intrinsic noise of ADC (Figure 5). For the 20 Hz data rate, the FIR filter with 8 Hz corner frequency will completely attenuate the quantization noise. (See also P. Lognonné et al, 2019)

Measured VBB channel performance

To illustrate the measured performance of the acquisition system, we compare the electrical noise of the acquisition channels obtained during the electrical tests with the seismic noise recorded during a very quiet period on Mars. The results are displayed in V/√Hz (amplitude spectrum density) and are referred to the inputs of the acquisition system.

When the E-Box is fully assembled, the inputs of the recording system are not accessible anymore. Therefore, we present noise results recorded during the electronics tests before integration of the sensor feedback electronics, i.e., during the so-called board level tests in the manufacturing phase. The test configuration only includes the AC part of the E-Box (see section ‘SEIS Electronics’). The corresponding spectra in the diagrams are labeled "Channel AC". The noise requirement for the acquisition channels is shown with the red line.

The right panel in Figure 6 shows the VBB velocity channels recorded with a sampling rate of 100 Hz. The Mars data was acquired on 2020-02-04 at 17:52 for 15 min (between 21:00-22:00 on Sol 423 – an extremely quiet time with minimal wind noise). The tick-noise artefact was removed from the Mars data (the tick-noise and the removal procedure is described in detail in section ‘1-Hz Mode (Tick-noise)’). In addition to the VBB sensor data, the acquisition system data, in which the sensor noise is not present, was acquired prior to the mission on 2014-10-16 for 15 min during the board level test of the FM electronics. The acquisition noise corresponds to the ADC intrinsic noise as shown in Figure 5 up to about 8 Hz. The ADC quantization noise

becomes dominant above 8 Hz and increases up to the corner frequency of the FIR filter, as explained in the section above.

In the left panel of Figure 6, VBB position channels with a sampling frequency of 1 Hz are compared. The Mars data was acquired on 2019-10-18 at 20:00 for 59 min, while the acquisition system data was recorded on 2014-10-04 for 59 min. Above ~0.15 Hz, the sensor noise becomes equal to or smaller than the acquisition noise.

Measured SP channel performance

The acquisition channels for the SP are identical to the VBB channels except that the full-scale range is reduced by half to ±12.5V. Therefore, the noise limit is lowered accordingly. Figure 7 shows the horizontal SP channels recorded during cruise on 2018-07-16 at 15:48 for 7 min and all three SP channels on Mars (2019-01-12 at 05:10 for 15 min), as well as the recorded acquisition channels during instrument board level test of the FM electronics on 2014-10-16 for 15 min, all with sampling frequency of 100 Hz. The cruise recordings show only the horizontal SP sensors as they work well in zero gravity environment. In contrast, the vertical SP sensor requires gravity to function. The shown noise spectra of the two horizontal SP sensors correspond to their self-noise, as there is no source of vibration on the spacecraft during cruise phase.

As explained in section ‘Channel Noise Performance’, and therefore expected, the ADC quantization noise dominates the acquisition noise above 8 Hz.

Linearity (INL)

As part of an instrument performance campaign, the Integral Non-Linearity (INL) of the acquisition channels on the flight spare (exact duplicate of the flight unit on Mars) was measured. A defined precise voltage V_{ref} was applied in steps to the differential inputs of the VBB channels (see block diagram in Figure 8). The voltages were acquired by the acquisition

electronics AC and additionally measured by a high-precision Digital Multi-Meter (DMM) to obtain a better knowledge about the input voltage. The measurements were carried out for all VBB channels before feedback board integration. For each tested input voltage, 10 seconds of data were sampled from all VBB channels at the highest sampling rate (i.e., 100 Hz for the velocity channels and 1 Hz for the position channels). The DMM was configured at fixed input range to maintain stable gain and offset during the test.

The analysis of the results was done separately for each VBB channel. First, the straight line between the range end-points is determined by calculating a gain and an offset, such that the digital number returned for the channel relates to the input voltage as follows:

1)

$$VBBchan = gain * V_{input} - offset$$

The offset and gain are determined by the following formulae:

2)

$$gain = \frac{VBBchan(20V) - VBBchan(-20V)}{V_{input}(20V) - V_{input}(-20V)}$$

3)

$$offset = VBBchan(-20V) - gain * V_{input}(-20V)$$

where the values between parentheses are the applied voltage. V_{input} refers to the value measured with the DMM. The endpoints of -20 V and +20 V correspond to the specified input voltage range.

For each input voltage set, the error is calculated:

4)

$$\varepsilon = VBBchan - gain * V_{input} - offset$$

The INL in percentage of the full-scale range using the maximum error measured, called ε_max:

5)

$$INL = 100 * \frac{\varepsilon\_max}{VBBchan(20V) - VBBchan(-20V)}$$

Figure 8 shows the measured errors for all VBB channels for the specified range extended by 10%, from which can be seen that the acquisition is still linear for signals slightly beyond the specified range.

The highest INL measured is about $3.2 \cdot 10^{-4}$ % for the VBB1 velocity channel, and this is well below $15 \cdot 10^{-4}$ %, the maximum INL in the ADC (AD7712) specification. A typical INL of $3 \cdot 10^{-4}$ % is specified for the ADC, and the results for all channels are close to this value. The non-linearity measured is according to what can be expected from the ADC. Thus, no significant contribution from the conditioning electronics is observed. However, we are also at the limits of the measurement setup itself. Therefore, the non-linearity observed may not only reflect the performance of the acquisition system, but also include limitations of the instrumentation and the setup used to obtain the result.

Temperature Acquisition Channels

There are three temperature measurement systems in the SEIS instrument:

- Scientific Temperature (SCIT A&B): Two thermistors (PT1000) mounted on the ring of the leveling structure. There are two, SCIT A and SCIT B, each connected to the corresponding AC side.
- VBB Engineering Temperature: Three thermistors, mounted on the three VBB sensors providing the sensor temperature
- Housekeeping Temperatures

Scientific Temperature (SCIT)

The SCIT is the tenth high-resolution channel of AC with a dedicated 24-bit ADC. Like the VBB POS channels, the SCIT is digitized with 32 kHz sample rate and provides, after ADC filtering and FIR filtering of the FPGA, the output rates of 1 Hz or 0.1 Hz. This high precision temperature measurement is implemented as a 4-wire measurement, meaning the two excitation lines to the thermistor are separated from the two sensing lines, to avoid voltage drop affecting the measurement due to long wires. Figure 9 shows the time-series (left) and the Amplitude Spectrum Density (ASD) (right) of measurements made during final testing of the E-Box FM electronics. In order to assess the performance of the circuit using a stable input signal, a resistor with a fixed and stable value replaced the temperature sensing thermistor.

The transfer function of the SCIT temperature measurement including the non-linear thermistor can be found in (P. Lognonné, 2019).

VBB Engineering Temperature (VBB[1,2,3] ENG TEMP)

The VBB engineering temperature measurement is a 2-wire measurement, using the same lines for excitation and sensing. Unlike the seismic channels and the SCIT that have a dedicated ADC, the three engineering temperature channels share a single ADC that acquires them in sequence. A multiplexer scans through all channels and a calibration resistor of 1 kΩ. For each channel and the calibration resistor, the ADC acquires 16 samples, which are averaged. In a second step, an offset compensation is applied with equation (6).

6)

$$\mathrm{VBBx_{Temp}} = \mathrm{VBBx_{avg}} + \left(\mathrm{RefConst} - \mathrm{Cal_{avg}}\right)$$

$\mathrm{VBBx_{Temp}}$ = Engineering Temperature Result for each channel, $x = 1 \ldots 3$

$\mathrm{VBBx_{avg}}$ = averaged 16 ADC samples for each channel, $x = 1 \ldots 3$

RefConst = Reference constant representing 1 kΩ

$$\mathrm{Cal}_{\mathrm{avg}} = \text{averaged 16 ADC samples measured on calibration resistor of 1 k}\Omega$$

In contrary to the SCIT channel that is a continuous stream, the VBB engineering temperature channels are a series of point measurements. There is no post-filtering as with the SCIT channel. The noise performance, measured at a sample rate of 1 Hz with a fix resistor, is 1.5 mK/√Hz over the frequency band from 0.5 Hz down to 0.01 mHz and is well below the requirement of 3 mK/√Hz.

The conversion factors including the non-linear thermistor can be found in (P. Lognonné, 2019).

Housekeeping Temperatures

The housekeeping temperatures are a third category of temperature measurements. They are designed to provide the temperatures of sensors and electronics boards in the instrument for diagnostic purposes. They are collected together with the voltage and current measurements with a resolution of 12-bits.

Time Base

The acquisition clock is derived from the AC master clock, which is based on the Hybrid Crystal Oscillator QT625LEM-32.768000MHz QTH U. The acquisition is therefore free-running with respect to the spacecraft clock and the Universal Time Coordinated (UTC). The oscillator temperature sensitivity is up to ~1 ppm/°C according manufacturer's temperature sensitivity curve. The estimated drift is then between -20 ppm and +5 ppm in the maximum temperature range of -35 ºC to +50 ºC specified for E-Box. The acquired data is time stamped with the Local On-Board Time (LOBT), which is derived as well from the master clock. This time is kept by a 40-bit counter with a resolution of 1/1024 s. The value of this counter is included as time stamp in the 1-second packets.

The time correlation between the LOBT and UTC is performed in post-processing. This is done in two steps. The LOBT is correlated with the spacecraft clock (SCLK). For this purpose, the AC

receives the spacecraft clock SCLK together with a synchronization pulse from the lander. This is used to generate pairs of LOBT/SCLK from the same instant in time, which are retrieved by the lander. Then the SCLK time is correlated with UTC using time pairs from the X-band communication.

Strategies to record information beyond the Nyquist frequency of 50 Hz

For specific seismic investigations, it is of interest to record seismic signals with a frequency content exceeding the effective bandwidth of 0 - 40 Hz (considering the low-pass -3dB corner) with a Nyquist frequency of 50 Hz dictated by the 100 Hz sampling frequency. For example, the eigen-modes of the LVL show eigen-frequencies >50 Hz (Lognonné et al., 2020). Furthermore, the hammering of the HP^3 mole into the ground to measure a vertical thermal conductivity profile will generate signals > 50 Hz that may allow inferring on elastic properties of the shallow Martian crust (Kedar et al., 2017; Golombek et al., 2018; Brinkman et al., 2019). Changing the FIR filters of stage 1 in the velocity signal acquisition chain (Figure 4 upper diagram) allows recording information outside the effective frequency bandwidth of 0 - 40 Hz.

A straightforward way to extend the bandwidth of SEIS is to exploit the fact that, following the Nyquist sampling theorem, the sampling limitations are not dictated by the maximum frequency, but by the bandwidth of the signal. Any signal that is constrained to a bandwidth of 50 Hz with a minimum frequency of an integer multiple of 50 Hz can therefore be exactly reconstructed when sampled at a sampling rate of 100 Hz. For example, changing the FIR filter of a velocity channel to pass 50 - 100 Hz at stage 1 will lead to the data being aliased once (Figure 10). The original information can then be recovered by re-mapping the information that mapped onto the 0 - 50 Hz band back to the 50 - 100 Hz band, resulting in an effective 200 Hz sampling frequency. If data from both the VBB (recording 0 - 50 Hz) and SP instrument (recording 50 - 100 Hz) are combined, a bandwidth from 0 to approximately 100 Hz can be covered. For technical reasons,

the FIR filters must have a DC gain of 1. Therefore, the FIR filter designed to record the 50 – 100 Hz band needs to exclude frequencies close to 100 Hz and in practice ranges from 56 to 87 Hz (-3dB), resulting in an effective bandwidth when combining both VBB and SP from 0 – 87 Hz with a notch at 50 Hz.

A second approach can be applied to repetitive signals with known characteristics, for which significant constraints apply. It is possible to set up inversion schemes to recover information that is aliased even by a few orders, thereby extending the recording bandwidth significantly beyond 50 Hz. Replacing the nominal FIR filter of stage 1 by a single spike will lead to a filter passing all frequencies (Sollberger et al., 2020). Subsequent down-sampling will result in the information being aliased up to several orders. The original signals can be reconstructed by making use of the fact that the HP^3 hammering waveform data are characterized by a high number of similar signals generated by each mole hit. Additionally, the hammering is not synchronized with the seismic data sampling so that over the repetitions of the signal the samples spread randomly over time, and this allows recovering the full information content up to a sample rate of 500 Hz (Sollberger et al., 2020). The FIR filter coefficients are implemented in the AC as signed 32-bit integer numbers, followed by a scaling of 2^{-32}. The spike filter is realized by setting all coefficients to zero except one that is set to the maximum value resulting in a filter with a gain of $(2^{31} - 1)/(2^{32}) \approx 0.5$. Hence, the data acquired while this filter is applied need to be multiplied by a factor of 2 before the usual conversion from digital counts to volts is applied, which results in the loss of 1 bit of resolution (the nominal resolution is 24 bits).

Health Monitoring and Trend Analysis

Forty-seven housekeeping acquisition channels and numerous status and error flags of E-Box as well as information gathered by the lander provide information about the health of the instrument and especially of the E-Box. If an anomaly occurs, this information can be used to identify and

analyze the problem in order to decide on the corrective action necessary, such as changing the configuration or turning off a sub-system. In addition, by monitoring the health information, adverse trends can be detected before a problem or a defect develops.

The health monitoring gives confidence that the instrument electronics are functioning well. The actual health check system comprises nine current measurements, thirteen voltage measurements, twenty-three temperature measurements, the position measurements of the SP sensors, an analysis of the clock drift, and the evaluation of sixteen error flags and fourteen status flags. The monitoring system uses state dependent limits, i.e., the limits are set depending on the configuration of the instrument. This allows setting narrower limit bands and provides in addition a check whether the configuration is applied as expected. It significantly reduces the probability of missing anomalous behavior. The configuration of the instrument is determined from the status flags that are returned as part of the health check data.

Trend Analysis

Trend analyses are performed to analyze the long-term stability of the E-Box. It uses a special version of the health check that shows data from several days at the beginning of the period and several days at the end of the period. This facilitates spotting changes in both the average and spread for the parameters analyzed. Changes in the parameter values due to different configurations that are applied during the reporting interval are taken into account. So far, two reports have been created during the operation on Mars, one for the period from 2019-03-11 to 2019-10-15, and the second for the period from 2019-10-14 to 2020-10-05. The results can be summarized as follows.

Voltages and Currents: The configuration changes that are relevant for the E-box voltages and currents during both periods were the switching on and off of the SA heating. The heating was switched on on 2019-05-18. As expected, the current of the + 7V supply increased with the

additional heating current. The heating was switched off on 2020-07-18, which reduced the current again to its initial value. No significant change over time was observed for any other of the currents and voltages.

Digital status / error flags: For the status and error flags, a trend analysis is not applicable. The analysis of the error and status flags in the full reports showed that no error flags were triggered in either of the reported periods. This means that no over-currents have occurred that would have resulted in sub-systems being switched off. No samples were marked invalid for any reason other than overflow in one of the FIR stages, which can also occur during FIR filter settling if a channel is activated. Furthermore, no adverse radiation effects on the operational amplifiers used for the conditioning of the seismic sensor signals were encountered. There was no radiation related disruption in the ADC, which is detected and flagged accordingly by the ADC controller, and thus its synchronization and calibration was established and retained throughout the active period.

Memory data retention: Only few single-bit errors occurred in the FLASH memory within both periods. The FLASH controller corrects these errors, i.e., they do not result in loss of scientific data. The frequency at which these errors have occurred since landing on Mars is at the expected rate and not increasing. No double-bit errors, which cannot be corrected by the FLASH controller, have occurred in the FLASH memory.

The FIR coefficients were always read before the FIR filters were updated or reconfigured and each time the read coefficients were identical to those previously programmed. Thus, there was no data retention problem for the FIR coefficients.

LOBT drift versus SCLK: Figure 11 shows the LOBT drift w.r.t. the SCLK in parts per million for the last reporting period. No significant difference over time is observed, although the negative peaks seem to be more pronounced in the last set of days. This difference correlates

with the temperature of the crystal used for the LOBT. The frequency of this crystal is maximum at 0 ° C and thus decreases when the temperature is lower. The temperature's diurnal cycle stays above -15 °C for the first two sets of days, but has minima as low as -20 °C in the last set of days. These lower temperatures explain the more pronounced minima in the last set of days. The maximum drift of the LOBT w.r.t SCLK is around 3.5 ppm in both reporting periods. No significant change over time could be observed. The limits shown in the plot take into account the entire temperature range in which the E-Box can operate, i.e., from -35 °C to +50 °C.

LVL-MDE communication: The full reports have shown that communication with the LVL-MDE was always successful in the reported periods. This can be confirmed by the acknowledge messages received from the LVL-MDE.

Summary: In both periods, i.e., during the entire scientific operation on Mars, no anomaly or adverse trend was found in the E-Box.

1-Hz Mode (Tick-noise)

The seismic data acquired by the SEIS instrument show a very small but constant 1 Hz signal with its higher harmonic modes (subsequently denoted as "tick-noise") as an artefact on all the VBB and SP velocity channels. The amplitude of the tick-noise is of order up to fifty µVrms at the various acquisition system inputs (referring to a full-scale of ±12.5 V for SP and ±25 V for VBB). The tick-noise is produced by cross-coupling from switching signals to the sensitive sensor lines that carry the seismic signal, which are routed in parallel through the sensor feedback boards and the 3-meter-long tether down to the sensor assembly. The aggressor signals belong to temperature measurements that are driven by the AC. Currents are being sent through various thermistors in the VBB sensors and their front-end electronics to measure the resulting voltages representing the temperatures. These measurements are cycled through the thermistors,

i.e., the signals are switched to each of the thermistors one after the other, every second. This on-off current switching produces transients on the sensor lines at a 1 s repetition rate, resulting in the observed tick-noise. A detailed investigation on the flight spare acquisition and control electronics confirmed that the shapes of the tick-noise could be traced back to the switching instants of the different temperature measurement channels. The tick-noise is most evident during periods of low seismic noise and appears as peaks in the frequency spectrum or as horizontal lines in spectrograms. The tick noise is also prominent in spectrum density charts of longer measurements, where the frequency bins become very narrow, because all its energy is concentrated in a few bins. Examples of tick-noise are shown in Figure 12 and discussed in more detail in the following section.

Investigation and characterization

From the beginning of operations on Mars, the tick-noise was monitored as one of the routine health-check tasks of the SEIS instrument. First on a weekly basis, then every month, the VBB and SP velocity signals are stacked and the amplitude spectra calculated. Then they are manually compared with previous stacks. The objective is to identify, over long term, any instability or continuing trend of tick-noise's amplitude or shape. The following information summarizes the findings so far.

In Figure 12 we see the amplitude spectra and in Figure 13 the stacked waveforms of the SEIS velocity channels, recorded in 2019 and 2020 with a 20 Hz sampling rate and configured in high gain, the most common configuration for continuous acquisition on Mars. The left side of Figure 12 shows frequency spectra of the recordings of the three SP channels over 24 hours. The rms (root-mean-square) amplitudes of the tick-noise, calculated from the samples of the stacked signal, vary from channel to channel in the range of 3.9 to 7.5 µV, at a SP full-scale range of ±12.5 V.

Figure 13 left side shows the tick-noise shapes resulting from stacking the signals of SP recordings on 2019-07-22, 2020-01-03 and 2020-08-28. The stacked signal is always 1 second long, i.e., the number of samples in the stack equals the sampling rate. Note that the peak amplitudes do not change significantly over one year's period between the different recordings. The shapes and amplitudes of SP1 and SP3 are rather invariant over time. The SP2 has a much smaller peak and thus shows larger variation due to the presence of the overall-noise.

The amplitude spectrum charts in Figure 12 right side show the VBB channels, recorded on 2020-07-04 over 24 hours. The rms amplitudes of the tick-noise vary from channel to channel from 7.5 μV_{rms} up to 49 μV_{rms}, the latter due to the significantly larger peak on VBB2. The VBB full-scale range is ±25 V.

Figure 13 right side shows stacked VBB waveforms from 2019-06-04, 2020-01-03 and 2020-07-04. As for the SP channels, the peak amplitudes do not change significantly over one year's period between the different recordings. The shape and amplitude of VBB2 is almost identical. VBB1 and VBB3 have no distinct peak and show some degree of shape variability, as the signal is very small w.r.t. the overall noise.

The VBB channels configured in low gain are rarely used and only for special purposes. Therefore, there are only short records available. To assess how the tick noise affects this configuration, waveforms for all three VBB channels were recorded for 40 minutes on January 19, 2020. No 1-Hz peaks are visible in the spectra of VBB1 and VBB2 because they fall below the noise floor of the sensors. VBB2 shows a peak at 1 Hz, of which the rms amplitude is 17.6 µVrms, thus roughly a factor of three smaller than the 49.2 µVrms of VBB2 in high gain. This reflects the gain difference between high and low gain (see P. Lognonné, 2019) and indicates that the crosstalk injection point is in front of the gain stage. The gain selection is part of the velocity signal output amplifier of the VBB sensor feedback electronics and thus just in

front of the acquisition electronics. In the remaining VBB channel configuration modes, i.e., VBB engineering (ENG) at high and low gain, and SP low gain, the tick-noise is not visible due to the higher sensor noise floor.

In the commissioning phase, the tick-noise appeared as well with a frequency of 0.1 Hz when the temperature measurements were configured to run at a rate of 10 seconds. The effect and root cause is the same as described above. The project decided that this configuration should no longer be used for the science operation of the instrument.

Tick-noise removal

We suggest removing the tick-noise by subtracting the repetitive 1 Hz signal from the recorded waveform in the time domain. In a first step, we determine the tick-noise waveform by stacking consecutive 1-second chunks from the continuous waveform (i.e., the number of samples per chunk equals the sampling rate). Through this stacking process, the random noise is averaged and thus reduced while the periodic tick-noise is averaged to its amplitude. The result is a waveform of 1 second length, which contains the disturbing tick-noise waveform (see Figure 13).

The stacking process can be expressed in following equation:

7)

$$stackSample(i) = \frac{\sum_{m=0}^{n-1} sample(t+sampleRate*m)}{n}, n = 1 \dots number\ of\ stacks$$

8)

$$number\ of\ stacks = \frac{waveform\ in\ seconds}{sample\ rate}$$

9)

$$Number\ of\ samples\ in\ stacked\ waveform = sampleRate$$

The longer the waveform we are processing, the better the averaging of the random noise and the cleaner the shape of the tick-noise we obtain.

In a second step, the offset (i.e., the mean of the samples) is removed from the stacked waveform, as it is not a part of the disturbing signal.

In a third step, this tick-noise waveform is subtracted from the continuous waveform second by second in exact phase. After subtraction, the resulting waveform is tick-noise free.

The waveform correction becomes:

10)

$$corrSample(i) = sample(i) - stackSample(i - sampleRate * m)\ , for\ m = 0 \ldots n - 1$$

To achieve a successful removal of the tick-noise, one must take into account the following considerations:

a) Use continuous waveforms without gaps
b) Subtract exactly in phase, i.e., subtract the stacked waveform from the same 1 second long chunks that were used in the stacking process
c) The quality of the tick-noise removal depends on the averaging process. Although the suggested tick-noise removal works well with records as short as 20 minutes, longer waveforms are providing improved results

The result of the tick-noise removal works well for most waveforms, including waveforms with sampling rates of 100 Hz. However, the removal may not work satisfactory on shorter waveforms with large drift and/or numerous glitches (Scholz et al., 2020). The stacked waveforms will not be accurate and therefore the tick-noise removal becomes insufficient. Running the removal process on a strongly drifting signal without high-pass filtering results in a waveform with only slightly reduced tick-noise. Filtering of the waveform before stacking, for example with a first-order high-pass filter with a corner frequency at 0.1 Hz, leads to an improved result.

Numerous glitches and strongly varying noise amplitudes prevent the waveform from being averaged properly, making the correction imperfect. A significant improvement can be achieved by using only those data chunks for the stacking process that contain no glitches or only glitches with small amplitudes. This is implemented by calculating the variance of each 1-second chunk and comparing it to a defined threshold value. The threshold has to be found experimentally. In the example in Figure 14, a variance threshold of 10^{+4} was chosen to obtain a more accurate peak shape (chart on the right hand side). Approximately 11% of 2880 data chunks exceeded the threshold and were not used for the stacking process.

Figure 15 shows the resulting waveform with the removed tick-noise. Re-stacking an already "cleaned up" waveform reveals remaining tick noise with an RMS amplitude less than 1 count. This tick-noise residual can be further reduced by applying a dither, i.e., by adding a random fraction of a count to each sample, before writing to the mini seed file. For example, applying a dither of ±0.5 count (peak to peak) to the waveform in Figure 15 reduces the remaining tick-noise rms amplitude from 0.29 counts to 0.0073 counts.

Alternative approaches for removing the tick noise could be used, for example, a method in the frequency domain could replace the spectral amplitudes at the peaks with the mean of immediate neighboring frequency bands.

Conclusions

Electronics development for planetary space projects is challenging. The enormous vibration imposed during launch and the large shocks while landing on the planet mechanically stress the electronics assembly. The performance must be maintained despite the large temperature variations during operations. The space radiation environment outside the protective magnetosphere of Earth can have damaging effects on the electronics components. Limited

power available for planetary missions requires careful balancing and tradeoff between low power design and performance. In order to ensure the successful operation, the requirements with respect to the environment in which the electronics has to perform and sustain are therefore very stringent. The equipment is thoroughly tested before it is accepted for the mission, using temperature ranges that extend well beyond those expected during the real operation. The design must take into account the limited choice of electronics components that are sufficiently thermo-mechanically robust and radiation tolerant. Compromises were made, such as accepting an increased noise at higher frequencies by selecting the 24-bit ADC for the acquisition that in turn has the required radiation tolerance, which was already proven in flight prior to this mission. SEIS electronics was successfully commissioned and has now been operating for more than two years on Mars without any anomalies, acquiring seismic data with a resolution and a dynamic range that is unprecedented in planetary seismology.

The described tick-noise artefact is an unwanted signal that was discovered in the integration phase of the development process, too late to take remedial action. The cause is not a problem of a specific point in the electronics, but rather a problem related to the large instrument layout (acquisition electronics – 3m-tether – sensor assembly). Fortunately, the tick-noise is stable and this paper proposes a method that shows its successful removal by post-processing the data.

Glossary

AC	Acquisition and Control electronics
ACQ	Acquisition Electronics board
ADC	Analog-to-Digital Converter
APSS	Auxiliary Payload Sensor Suite
C&DH	Command and Data Handling unit

616	CTL	Control Electronics board
617	DC	Power Distribution and Conditioning Electronics board
618	DMM	Digital Multi-Meter
619	E-Box	Electronics Box
620	FIR	Finite Impulse Response filter
621	FPGA	Field Programmable Gate Array
622	FLASH	non-volatile memory
623	FM	Flight Model
624	HP^3	Heat Flow and Physical Properties Package
625	INL	Integral Non-Linearity
626	InSight	Interior exploration using Seismic Investigations, Geodesy and Heat Transport
627	LOBT	Local On-Board Time
628	LVL	Leveling Structure
629	LVL-MDE	Leveling Motor Drive Electronics
630	PDDU	Power Distribution & Drive Unit
631	PDS	Planetary Data System
632	RISE	Rotation and Interior Structure Experiment
633	RWEB	Remote Warm Enclosure Box
634	SCIT	Scientific Temperature
635	SCLK	Spacecraft Clock
636	SEIS	Seismic Experiment for Interior Structure
637	SA	Sensor Assembly
638	SP	Short Period sensors
639	SP-FB	SP Feedback board

UTC	Universal Time Coordinated
VBB	Very-Broadband sensors
VBB-FB	VBB Feedback board
WEB	Warm Electronics Box
WTS	Wind and Thermal Shield

Data and Resources – see detailed information below

Tick-Noise Removal Implementation in MATLAB and PYTHON code

The function TICKREM is provided in MATLAB and PYTHON code, available for download in the electronic supplement to this article. It reads a mini seed file, corrects it and writes another mini seed file. For mini seed read and write, the MATLAB version calls the functions RDMSEED and MKMSEED, downloadable from MathWorks web site [https://ch.mathworks.com/matlabcentral/fileexchange/28803-rdmseed-and-mkmseed-read-and-write-miniseed-files].

The read and write file names and corresponding directory paths can be specified in the arguments. The stacking and the removal process is performed in double precision floating point, but rounded to integer before writing to the mini seed file. The result is written to the same SEED compression format as read (Note: only Steim1 and Steim2 are implemented).

There are three other arguments that control the correction function. The argument [hp_filt] sets the corner frequency of the first-order high-pass filter in Hz. The value [0] will switch-off the filter, the recommended default value is [0.1] Hz. The argument [var_threshold] defines the threshold that defines up to which variance level the waveform chunk is used for the stacking process. Chunks with a variance level higher than [var_threshold] are disregarded (refer to section [Tick-noise removal]). The recommended default value is [10^{+05}]. Finally, the argument

664 [dither], which further reduces the residual of the tick-noise by applying and thus randomizing
665 the waveform. The recommended value is [1.0], which corresponds to a dither of ±0.5 count. The
666 value set to zero will switch-off the dither.
667 The default values are suitable for most waveforms.
668
669 The InSight mission raw and calibrated data sets are available via NASA's Planetary Data
670 System (PDS; National Aeronautics and Space Administration Planetary
671 Data System, https://pds.nasa.gov/; InSight Mars SEIS Data Service (2019)). Data are delivered
672 to the PDS according to the InSight Data Management Plan available in the InSight PDS archive.
673 All datasets can be accessed at https://pds-geosciences.wustl.edu/missions/ insight/index.html.
674

675 *Acknowledgments*

676 We acknowledge NASA, CNES and its partner agencies and institutions (UKSA, SSO,
677 DLR, JPL, IPGP-CNRS, ETHZ, IC and MPS-MPG) and the flight operations team at JPL,
678 SISMOC, MSDS, IRIS-DMC and PDS for providing SEIS data. The Swiss co-authors were
679 jointly funded by (1) the Swiss National Science Foundation and French Agence
680 Nationale de la Recherche (SNF-ANR project 157133 'Seismology on Mars'), (2) the
681 Swiss National Science Foundation (SNF project 172508 'Mapping the internal structure of
682 Mars'), (3) the Swiss State Secretariat for Education, Research and Innovation, (4) ETH research
683 grant ETH-06 17-2. This is InSight contribution number 208.
684

685 *References*

686 Banerdt, W. B., S. Smrekar, D. Banfield, D. Giardini, M. Golombek, C. Johnson, P. Lognonné,
687 A. Spiga, T. Spohn, C. Perrin, S. Stähler, D. Antonangeli, S. Asmar, C. Beghein, N.

Bowles, E. Bozdag, P. Chi, U. Christensen, J. Clinton, G. Collins, I. Daubar, V. Dehant, M. Drilleau, M. Fillingim, B. Folkner, R. Garcia, J. Garvin, J. Grant, M. Grott, J. Grygorczuk, T. Hudson, J. Irving, G. Kargl, T. Kawamura, S. Kedar, S. King, B. Knapmeyer-Endrun, M. Knapmeyer, M. Lemmon, R. Lorenz, J. Maki, L. Margerin, S. McLennan, C. Michaut, D. Mimoun, A. Mittelholz, A. Mocquet, P. Morgan, N. Mueller, S. N. Murdoch, Nagihara, C. Newman, F. Nimmo, M. Panning, T. Pike, A.-C. Plesa, S. Rodriguez, J.-A. Rodriguez-Manfredi, C. Russell, N. Schmerr, M. Siegler, S. Stanley, E. Stutzmann, N. Teanby, J. Tromp, M. van Driel, N. Warner, R. Weber, and M. Wieczorek, Initial results from the InSight mission on Mars. Nat. Geosci. 13, 183–189 (2020). https://doi.org/10.1038/s41561-020-0544-y

Banfield, D., J.A. Rodriguez-Manfredi, C.T. Russell, K.M. Rowe, D. Leneman, H.R. Lai, P.R. Cruce, J.D. Means, C.L. Johnson, S.P. Joy, P.J. Chi, I.G. Mikellides, S. Carpenter, S. Navarro, E. Sebastian, J. Gomez-Elvira, J. Torres, L. Mora, V. Peinado, A. Lepinette, K. Hurst, P. Lognonné, S.E. Smrekar and W.B. Banerdt, InSight Auxiliary Payload Sensor Suite (APSS). Space Sci. Rev. (2018). https://doi.org/10.1007/s11214-018-0570-x

Brinkman, N., C. Schmelzbach, D. Sollberger, M. van Driel, J. ten Pierick, J. O. A. Robertsson, F. Andersson, S. Kedar, M. Grott, T. Hudson, W. B. Banerdt, L. Fayon, A. Horleston, K. Hurst, A. Kiely, B. Knapmeyer-Endrun, C. Krause, P. Lognonné, W. T. Pike, S. Stähler, T. Spohn, and N. Teanby (2019), The first active-seismic experiment on Mars to characterize the shallow subsurface structure at the InSight landing site, SEG Technical Program Expanded Abstracts 2019, 4756–4760, doi:10.1190/segam2019-3215661.1

S. Ceylan, J.F. Clinton, D. Giardini, M. Böse, C. Charalambous, M. van Driel, A. Horleston, T. Kawamura, A. Khan, G. Orhand-Mainsant, JR. Scholz, S. Stähler, F. Euchner, W.B. Banerdt, P. Lognonné, D. Banfield, E. Beucler, R.F. Garcia, S. Kedar, M.P. Panning, W.T. Pike, S.E. Smrekar, A. Spiga, N.L. Dahmen, K. Hurst, A.E. Stott, R. D. Lorenz, M. Schimmel, E. Stutzmann, J. ten Pierick, V. Conejero, C. Pardo, C. Perrin, (2020), Companion guide to the Marsquake catalog from InSight, sols 0–478: Data content and non-seismic events, Physics of the Earth and Planetary Interiors. https://doi.org/10.1016/j.pepi.2020.106597

Folkner, W.M., V. Dehant, S. Le Maistre, M. Yseboodt, A. Rivoldini, T. Van Hoolst, S.W. Asmar, M.P. Golombek, The Rotation and Interior Structure Experiment on the InSight Mission to Mars, Space Sci. Rev., 214:100, 2018. doi:10.1007/s11214-018-0530-5

Golombek, M., M. Grott, G. Kargl, J. Andrade, J. Marshall, N. Warner, N.A. Teanby, V. Ansan, E. Hauber, J. Voigt, R. Lichtenheldt, B. Knapmeyer-Endrun, I.J. Daubar, D. Kipp, N. Muller, P. Lognonne´, C. Schmelzbach, D. Banfield, A. Trebi-Ollennu, J. Maki, S. Kedar, D. Mimoun, N. Murdoch, S. Piqueux, P. Delage, W.T. Pike, C. Charalambous, R. Lorenz, L. Fayon, A. Lucas, S. Rodriguez, P. Morgan, A. Spiga, M. Panning, T. Spohn, S. Smrekar, T. Gudkova, R. Garcia, D. Giardini, U. Christensen, T. Nicollier, D. Sollberger, J. Robertsson, K. Ali, B. Kenda and W. B. Banerdt (2018), Geology and Physical Properties Investigations by the InSight Lander, Space Science Review, 214(5), 84, 10.1007/s11214-018-0512-7.

Kedar, S., Andrade, J., Banerdt, B., Delage, P., Golombek, M., Grott, M., T. Hudson, A. Kiely, M. Knapmeyer, B. Knapmeyer-Endrun, C. Krause, T. Kawamura, P. Lognonné, W.T. Pike, Y. Ruan, T. Spohn, N. Teanby, J. Tromp and J. Wookey (2017). Analysis of Regolith Properties Using Seismic Signals Generated by InSight's HP^3 Penetrator. Space Science Reviews, 211, 315–337. doi: 10.1007/s11214-017-0391-3

P. Lognonné, W.B. Banerdt, D. Giardini, W.T. Pike, U. Christensen, P. Laudet, S. de Raucourt, P. Zweifel, S. Calcutt, M. Bierwirth, K.J. Hurst, F. Ijpelaan, J.W. Umland, R. Llorca-Cejudo, S.A. Larson, R.F. Garcia, S. Kedar, B. Knapmeyer-Endrun, D. Mimoun, A. Mocquet, M.P. Panning, R.C. Weber, A. Sylvestre-Baron, G. Pont, N. Verdier, L. Kerjean, L.J. Facto, V. Gharakanian, J.E. Feldman, T.L. Hoffman, D.B. Klein, K. Klein, N.P. Onufer, J. Paredes-Garcia, M.P. Petkov, J.R. Willis, S.E. Smrekar, M. Drilleau, T. Gabsi, T. Nebut, O. Robert, S. Tillier, C. Moreau, M. Parise, G. Aveni, S. Ben Charef, Y. Bennour, T. Camus, P.A. Dandonneau, C. Desfoux, B. Lecomte, O. Pot, P. Revuz, D. Mance, J. tenPierick, N.E. Bowles, C. Charalambous, A.K. Delahunty, J. Hurley, R. Irshad, H. Liu, A.G. Mukherjee, I.M. Standley, A.E. Stott, J. Temple, T. Warren, M. Eberhardt, A. Kramer, W. Kühne, E.-P. Miettinen, M. Monecke, C. Aicardi, M. André, J. Baroukh, A. Borrien, A. Bouisset, P. Boutte, K. Brethomé, C. Brysbaert, T. Carlier, M. Deleuze, J.M. Desmarres, D. Dilhan, C. Doucet, D. Faye, N. Faye-Refalo, R. Gonzalez, C. Imbert, C. Larigauderie, E. Locatelli, L. Luno, J.-R. Meyer, F. Mialhe, J.M. Mouret, M. Nonon, Y. Pahn, A. Paillet, P. Pasquier, G. Perez, R. Perez, L. Perrin, B. Pouilloux, A. Rosak, I. Savin de Larclause, J. Sicre, M. Sodki, N. Toulemont, B. Vella, C. Yana, F. Alibay, O.M. Avalos, M.A. Balzer, P. Bhandari, E. Blanco, B.D. Bone, J.C. Bousman, P. Bruneau, F.J. Calef, R.J. Calvet, S.A. D'Agostino, G. de los Santos, R.G. Deen, R.W.

759 Denise, J. Ervin, N.W. Ferraro, H.E. Gengl, F. Grinblat, D. Hernandez, M. Hetzel, M.E.
760 Johnson, L. Khachikyan, J.Y. Lin, S.M. Madzunkov, S.L. Marshall, I.G. Mikellides, E.A.
761 Miller, W. Raff, J.E. Singer, C.M. Sunday, J.F. Villalvazo, M.C. Wallace, D. Banfield,
762 J.A. Rodriguez-Manfredi, C.T. Russell, A. Trebi-Ollennu, J.N. Maki, E. Beucler, M.
763 Böse, C. Bonjour, J.L. Berenguer, S. Ceylan, J. Clinton, V. Conejero, I. Daubar, V.
764 Dehant, P. Delage, F. Euchner, I. Estève, L. Fayon, L. Ferraioli, C.L. Johnson, J.
765 Gagnepain-Beyneix, M. Golombek, A. Khan, T. Kawamura, B. Kenda, P. Labrot, N.
766 Murdoch, C. Pardo, C. Perrin, L. Pou, A. Sauron, D. Savoie, S. Stähler, E. Stutzmann,
767 N.A. Teanby, J. Tromp, M. van Driel, M. Wieczorek, R. Widmer-Schnidrig, J. Wookey
768 (2019). SEIS: Insight's seismic experiment for internal structure of Mars.
769 https://doi.org/10.1007/s11214-018-0574-6
770
771 Lognonné, P., W. B. Banerdt, W. T. Pike, D. Giardini, U. Christensen, R. F. Garcia, T.
772 Kawamura, S. Kedar, B. Knapmeyer-Endrun, L. Margerin, F. Nimmo, M. Panning, B.
773 Tauzin, J. R. Scholz, D. Antonangeli, S. Barkaoui, E. Beucler, F. Bissig, N. Brinkman,
774 M. Calvet, S. Ceylan, C. Charalambous, P. Davis, M. van Driel, M. Drilleau, L. Fayon,
775 R. Joshi, B. Kenda, A. Khan, M. Knapmeyer, V. Lekic, J. McClean, D. Mimoun, N.
776 Murdoch, L. Pan, C. Perrin, B. Pinot, L. Pou, S. Menina, S. Rodriguez, C. Schmelzbach,
777 N. Schmerr, D. Sollberger, A. Spiga, S. Stähler, A. Stott, E. Stutzmann, S. Tharimena, R.
778 Widmer-Schnidrig, F. Andersson, V. Ansan, C. Beghein, M. Böse, E. Bozdag, J. Clinton,
779 I. Daubar, P. Delage, N. Fuji, M. Golombek, M. Grott, A. Horleston, K. Hurst, J. Irving,
780 A. Jacob, J. Knollenberg, S. Krasner, C. Krause, R. Lorenz, C. Michaut, B. Myhill, T.
781 Nissen-Meyer, J. ten Pierick, A.-C. Plesa, C. Quantin-Nataf, J. Robertsson, L. Rochas, M.
782 Schimmel, S. Smrekar, T. Spohn, N. Teanby, J. Tromp, J. Vallade, N. Verdier, C.

783 Vrettos, R. Weber, D. Banfield, E. Barrett, M. Bierwirth, S. Calcutt, N. Compaire, C.
784 Johnson, D. Mance, F. Euchner, L. Kerjean, G. Mainsant, J. A. Rodriguez Manfredi, G.
785 Pont, P. Laudet, T. Nebut, S. de Raucourt, O. Robert, C. Russell, A. Sylvestre-Baron, S.
786 Tillier, T. Warren, M. Wieczorek, C. Yana, P. Zweifel, Constraints on the shallow elastic
787 and anelastic structure of Mars from InSight seismic data. Nat. Geosci., 13, 213–220
788 (2020). https://doi.org/10.1038/s41561-020-0536-y
789
790 Scholz, J.- R., R. Widmer-Schnidrig, P. Davis, P. Lognonné, B. Pinot, R. F. Garcia, F. Nimmo,
791 K. Hurst, S. Barkaoui, S. de Raucourt, L. Pou, B. Pinot, N. Compaire, G. Mainsant, A.
792 Cuvier, E. Beucler, M. Bonnin, R. Joshi, E. Stutzmann, M. Schimmel, A. Horleston, M.
793 Böse, S. Ceylan, J. Clinton, M. van Driel, T. Kawamura, A. Khan, S. C. Stähler, D.
794 Giardini, C. Charalambous, A. E. Stott, W. T. Pike, U. Christensen and W. B. Banerdt
795 (2020). Detection, analysis and removal of glitches from InSight's seismic data from
796 Mars. Earth and Space Science 7, e2020EA001317- T.
797 https://doi.org/10.1029/2020EA001317
798
799 Spohn, T., M. Grott, S. E. Smrekar, J. Knollenberg, T. L. Hudson, C. Krause, N. Müller. J.
800 Jänchen, A. Börner, T. Wippermann, O. Krömer, R. Lichtenheldt, L. Wisniewski, J.
801 Grygorczuk, M. Fittock, S. Reershemius, T. Spröwitz, E. Kopp, I. Walter, A.-C. Plesa, D.
802 Breuer, P. Morgan, W. B. Banerdt, The Heat Flow and Physical Properties Package (HP^3)
803 for the InSight Mission, Space Sci. Rev., 214:96, 2018. https://doi.org/10.1007/s11214-
804 018-0531-4
805

Sollberger, D., C. Schmelzbach, F. Andersson, J .O .A. Robertsson ,S. Kedar, W. B. Banerdt, N. Brinkman, J. Clinton, M. van Driel, R. Garcia, D. Giardini, M. Grott, T. Haag, T. L. Hudson, P. Lognonné, J. ten Pierick, W. T. Pike, T. Spohn, S. Stähler, P. Zweifel, (2020), Reconstruction of temporally aliased seismic signals recorded by the InSight Mars lander, submitted to Earth and Space Science, 10.1002/essoar.10502908.1

InSight Mars SEIS Data Service. (2019). SEIS raw data, Insight Mission. IPGP, JPL, CNES, ETHZ, ICL, MPS, ISAE-Supaero, LPG, MFSC. https://doi.org/10.18715/SEIS.INSIGHT.XB_2016

NASA InSight Web Site. Artist's rendering of the Sensor Assembly. Credit: NASA/JPL-Caltech/CNES/IPGP Download on https://mars.nasa.gov/resources/22107/cutaway-of-seis/?site=insight

Full mailing address for each author

W. Bruce	Banerdt	william.b.banerdt@jpl.nasa.gov	Jet Propulsion Laboratory / California Institute of Technology	4800 Oak Grove Drive	Pasadena, CA 91109	USA
Marco	Bierwirth	bierwirthm@mps.mpg.de	Max-Planck-Institute for Solar System Research, Göttingen	Justus-von-Liebig Weg 3	D-37077 Göttingen	Germany
Savas	Ceylan	savas.ceylan@erdw.ethz.ch	Eidgenössische Technische Hochschule Zürich / Institute of Geophysics	Sonneggstrasse 5	CH-8092 Zurich	Switzerland
John F.	Clinton	jclinton@sed.ethz.ch	Eidgenössische Technische Hochschule Zürich / Swiss Seismological Service	Sonneggstrasse 5	CH-8092 Zurich	Switzerland
Michel	Eberhardt	eberhardt@mps.mpg.de	Max-Planck-Institute for Solar System Research, Göttingen	Justus-von-Liebig Weg 3	D-37077 Göttingen	Germany
Fabian	Euchner	fabian.euchner@sed.ethz.ch	Eidgenössische Technische Hochschule Zürich / Swiss Seismological Service	Sonneggstrasse 5	CH-8092 Zurich	Switzerland
Domenico	Giardini	domenico.giardini@erdw.ethz.ch	Eidgenössische Technische Hochschule Zürich / Institute of Geophysics	Sonneggstrasse 5	CH-8092 Zurich	Switzerland
Thomas	Haag	thomas.haag@erdw.ethz.ch	Eidgenössische Technische Hochschule Zürich / Institute of Geophysics	Sonneggstrasse 5	CH-8092 Zurich	Switzerland
Philippe	Lognonné	lognonne@ipgp.fr	Institut de Physique du Globe de Paris	35 rue Hélène Brion	75205 Paris Cedex 13	France
Davor	Mance	davor.mance@retired.ethz.ch	Eidgenössische Technische Hochschule Zürich / Institute of Geophysics	Sonneggstrasse 5	CH-8092 Zurich	Switzerland
Tobias	Nicollier	tobias.nicollier@wsl.ch	Eidgenössische Forschungsanstalt WSL	Zürcherstrasse 111	CH-8903 Birmensdorf	Switzerland
William T.	Pike	w.t.pike@ic.ac.uk	Imperial College London	Exhibition Road	London SW7 2AZ	United Kingdom
Cedric	Schmelzbach	cedric.schmelzbach@erdw.ethz.ch	Eidgenössische Technische Hochschule Zürich / Institute of Geophysics	Sonneggstrasse 5	CH-8092 Zurich	Switzerland
David	Sollberger	david.sollberger@erdw.ethz.ch	Eidgenössische Technische Hochschule Zürich / Institute of Geophysics	Sonneggstrasse 5	CH-8092 Zurich	Switzerland

Simon	Stähler	simon.staehler@erdw.ethz.ch	Eidgenössische Technische Hochschule Zürich / Institute of Geophysics	Sonneggstrasse 5	CH-8092	Zurich	Switzerland
Jan	ten Pierick	jan.tenpierick@erdw.ethz.ch	Eidgenössische Technische Hochschule Zürich / Institute of Geophysics	Sonneggstrasse 5	CH-8092	Zurich	Switzerland
Martin	van Driel	vandriel@erdw.ethz.ch	Eidgenössische Technische Hochschule Zürich / Institute of Geophysics	Sonneggstrasse 5	CH-8092	Zurich	Switzerland
Peter	Zweifel	peter.zweifel@retired.ethz.ch	Eidgenössische Technische Hochschule Zürich / Institute of Geophysics	Sonneggstrasse 5	CH-8092	Zurich	Switzerland

Tables, with captions above each table

List of Figure Captions

Figures, with captions below each figure – high resolution figure files are not needed for the review process. They will be requested after your paper is accepted for publication.

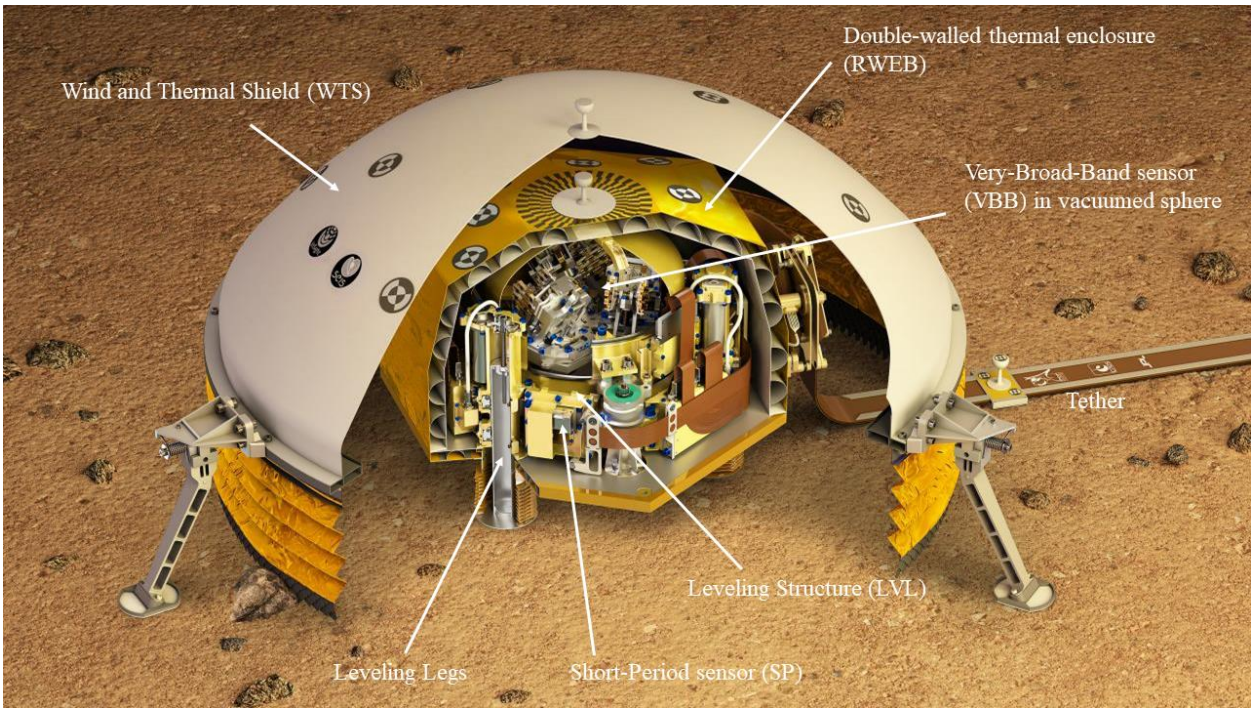

Figure 1 Artist' rendering showing a cutaway of the SEIS Sensor Assembly (SA) and the Wind and Thermal Shield (WTS). The leveling structure (LVL) was delivered by Max-Planck Solar System Research in Göttingen, Germany (MPS), the VBB sensor by the Institut du Physique du Globe in Paris, France, the SP sensors by Imperial College in London, UK, and the Wind and Thermal Shield (WTS) and tether by Jet Propulsion Laboratory (JPL) in Pasadena, USA. Credit: NASA/JPL-Caltech/CNES/IPGP (NASA InSight Web Site)

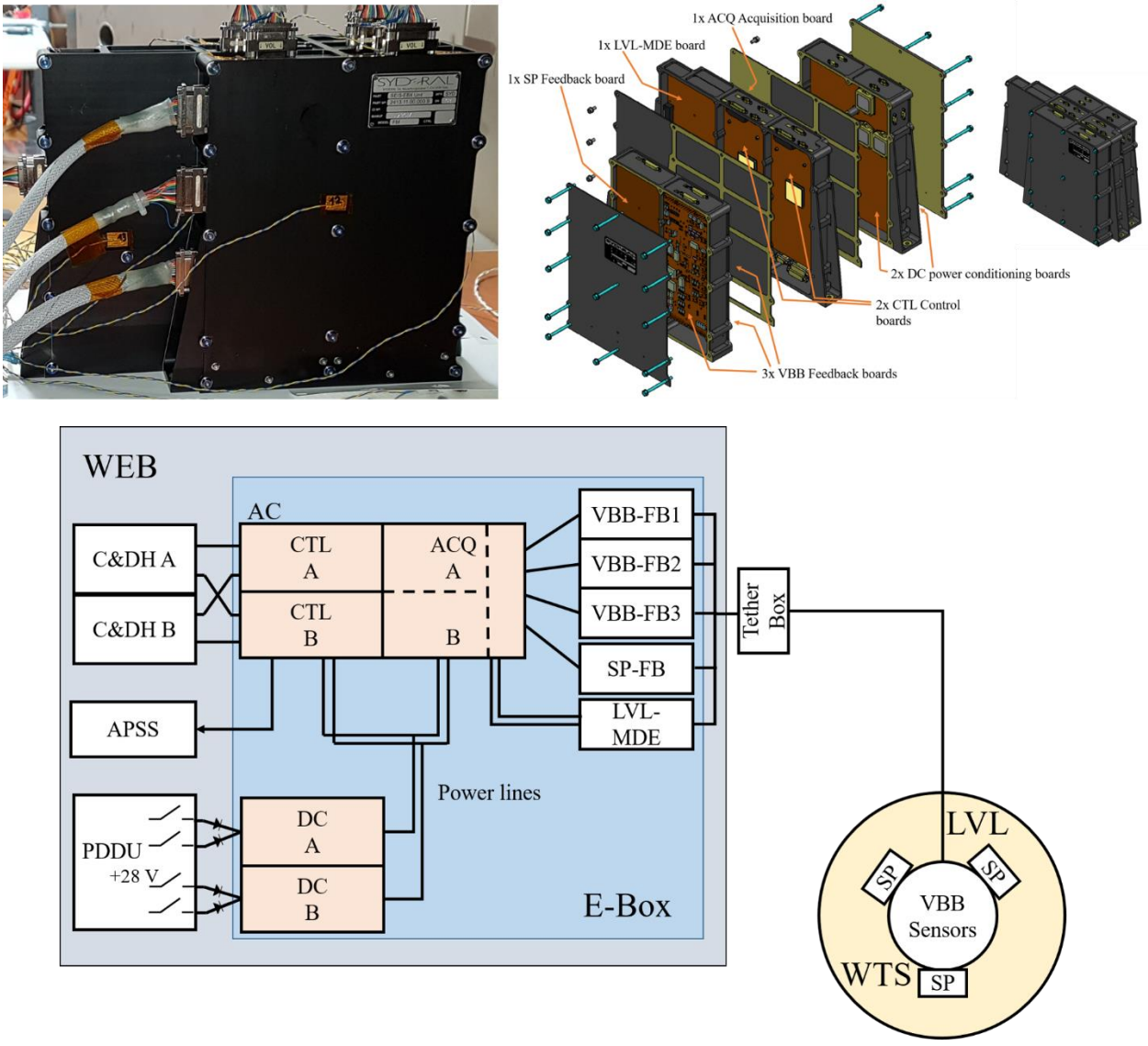

910

911 Figure 2 SEIS Electronics Box (E-Box) outside view, physical configuration and electrical
912 interconnections. The picture upper left shows the Flight Model (FM) unit, in preparation for the thermal
913 test. Dimensions: 244 mm (height), 170 mm (width), 344 mm (length); weight ~5 kg; E-Box was delivered
914 by ETH Zurich in Switzerland. The exploded view of the E-Box shows the board configuration: three
915 VBB-FB feedback boards (delivered by IPGP); one SP-FB feedback board (delivered by Oxford
916 University); one motor drive electronic board LVL-MDE (delivered by MPS); one ACQ acquisition board
917 (partially duplicated) and two duplicated control electronics boards CTL; two duplicated DC power boards,
918 condition the primary +28 V to all secondary voltages needed by the sub-systems (delivered by ETHZ).
919 Figure credit to Syderal SA, Switzerland, the manufacturer of the E-Box. The Block Diagram (lower part
920 of the figure) shows the interconnections within the SEIS instrument and to the external units Command &
921 Data Handling C&DH, the Power Distribution and Drive Unit PDDU and the Auxiliary Payload Sensor
922 Suite APSS (Banfield, 2018)

923

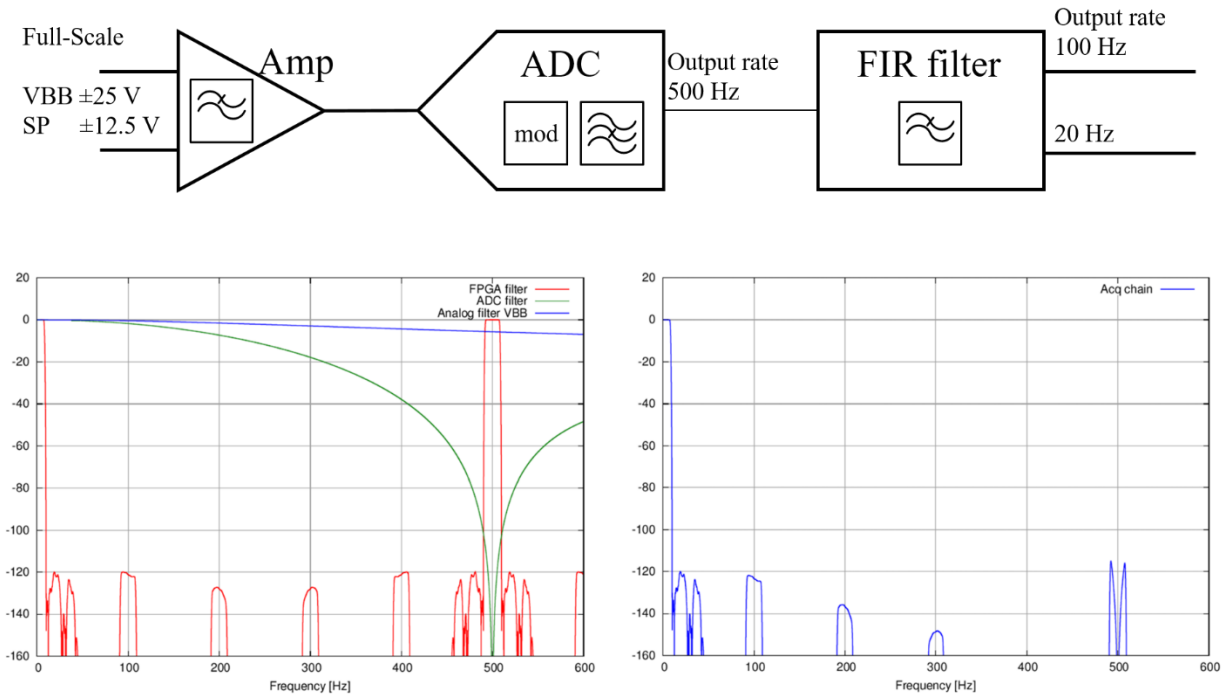

924

925 Figure 3 Acquisition chain with the anti-alias filter steps (block diagram on top). The charts show the
926 attenuation of the individual filters (left) and the attenuation combined (right) for the velocity chain at
927 20 Hz output rate.

928

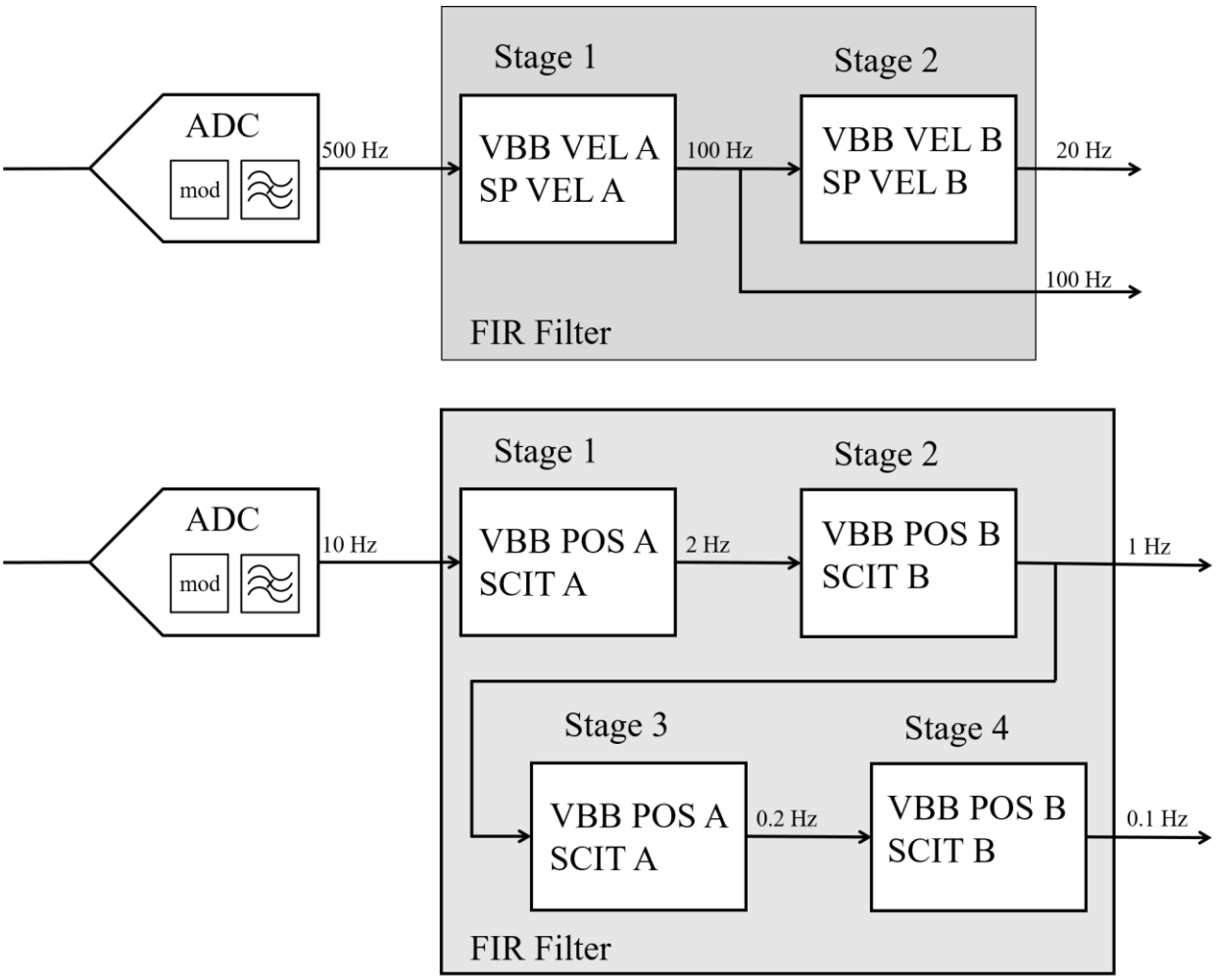

929

930 Figure 4 FIR filter stages for the VBB and SP velocity channels (upper diagram) and for the VBB position
931 and scientific temperature (SCIT) channels (lower diagram)

932

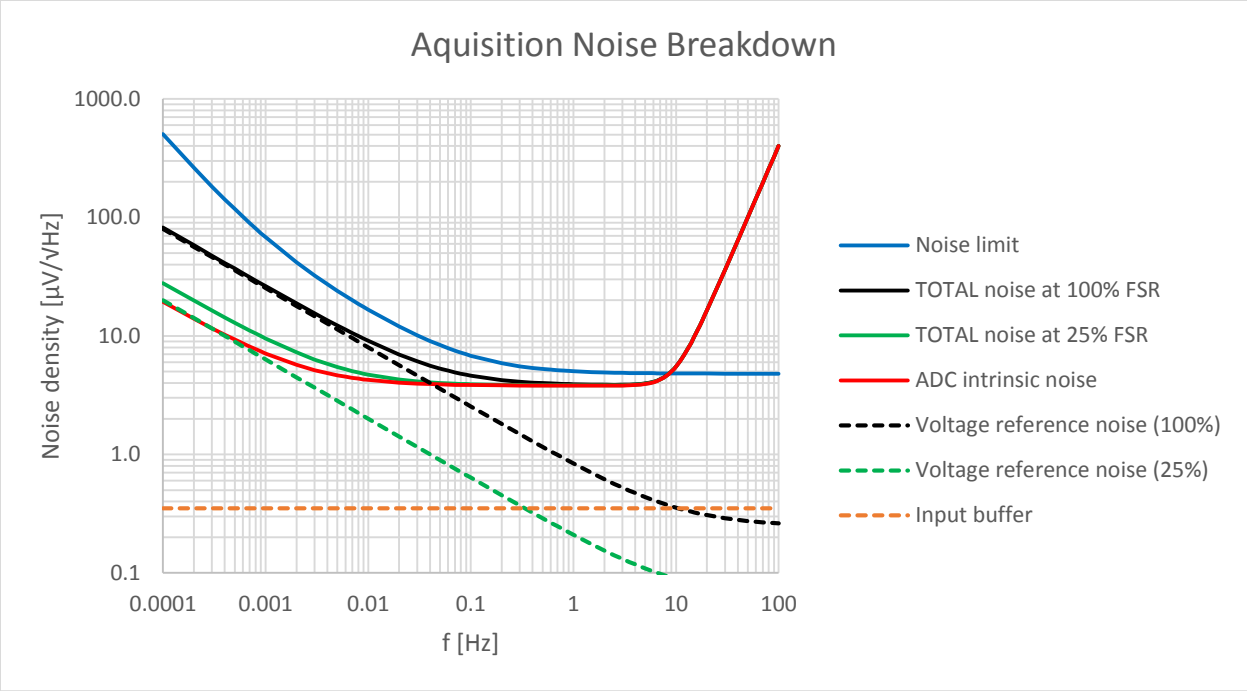

933

934 Figure 5 Acquisition Noise Breakdown of VBB velocity channel. (P. Lognonné, 2019)

935

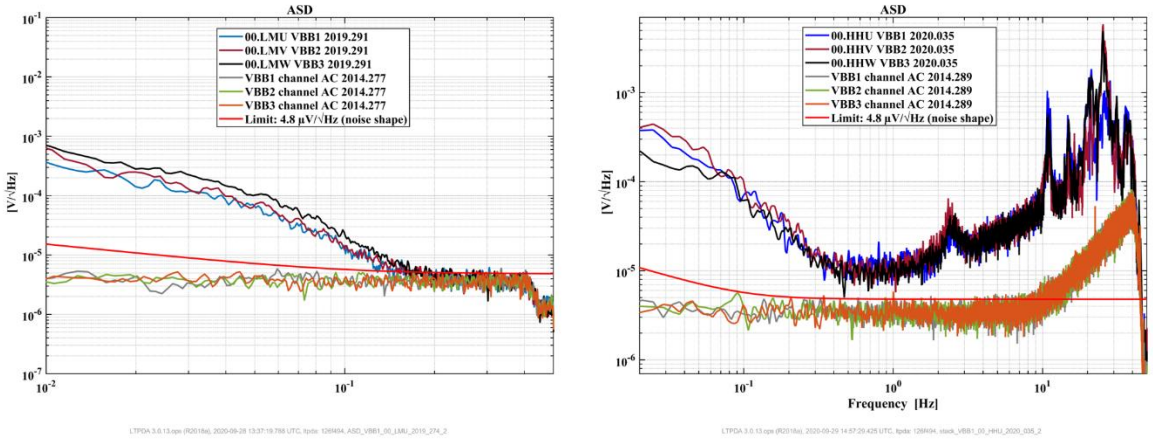

936

937 Figure 6 Noise Performance of VBB channels, compared to the acquisition system noise. VBB position
938 channels (left chart) at a sample rate of 1 Hz; recordings from 2019-10-18 at 20:00 for 59 min on Mars and
939 recordings obtained at board level test on 2014-10-04 for 59 min. VBB velocity channels (right chart) at a
940 sample rate of 100 Hz; recordings from 2020-02-04 at 17:52 for 15 min on Mars (event and recordings
941 obtained at board level test on 2014-10-16 for 15 min

942

943

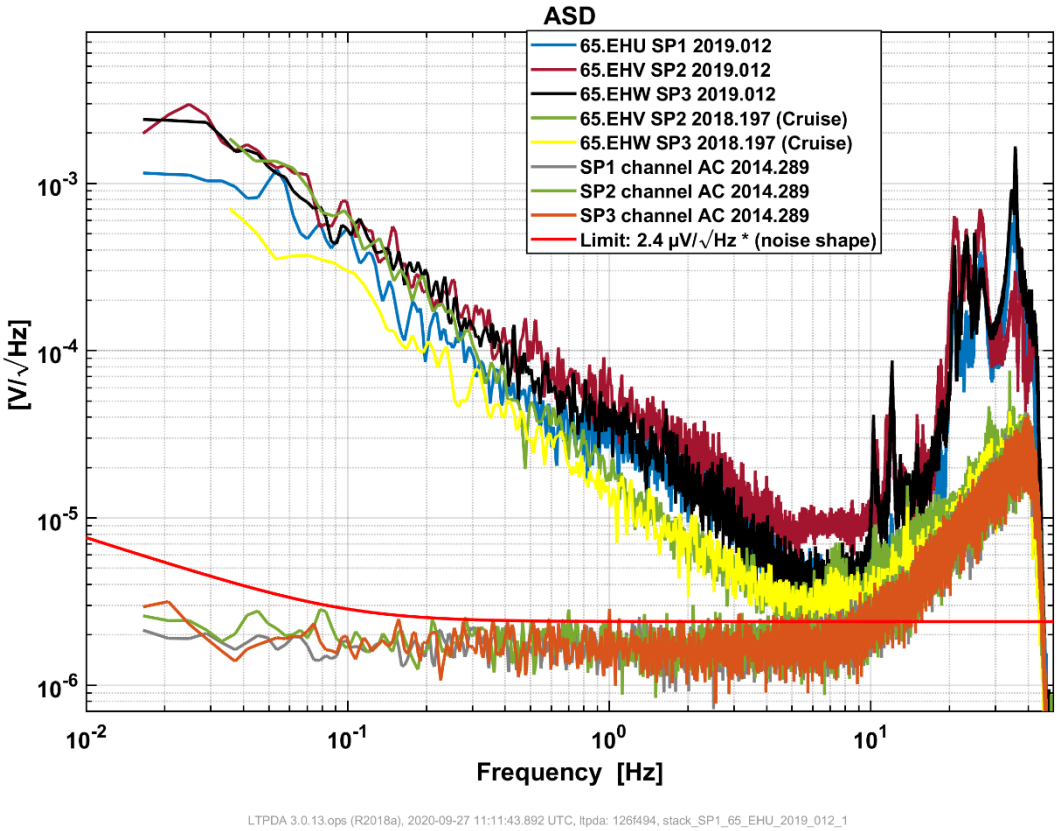

Figure 7 Noise Performance of SP velocity channels during cruise and on Mars, compared to the acquisition system noise; sample rate = 100 Hz; recordings from 2019-01-12 at 05:10 for 15 min on Mars, from 2018-07-16 at 15:48 for 7 min during cruise, and recordings obtained at board level test on 2014-10-16 for 15 min

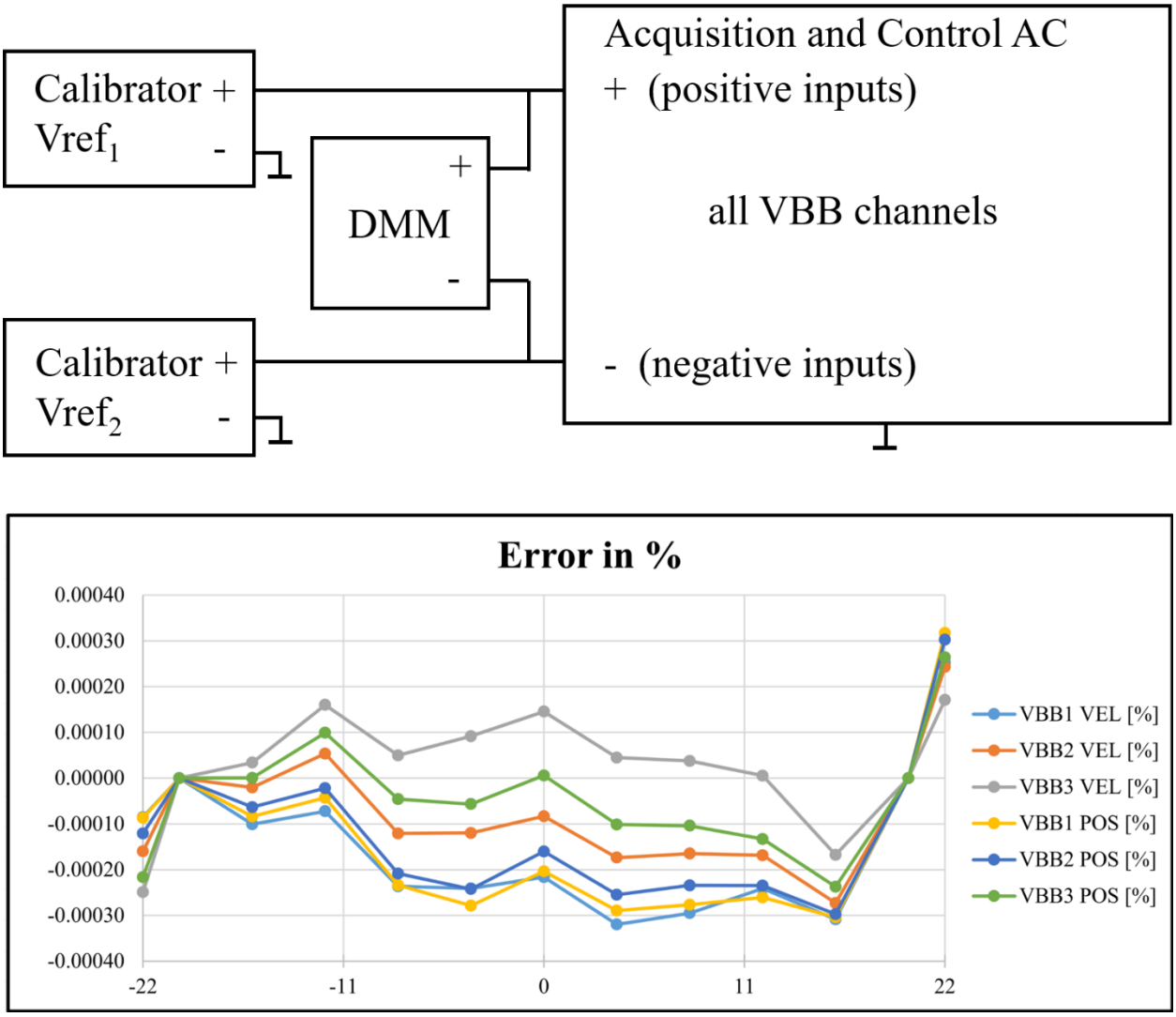

Figure 8 Linearity Measurement: Principal configuration (block diagram) and measurement results

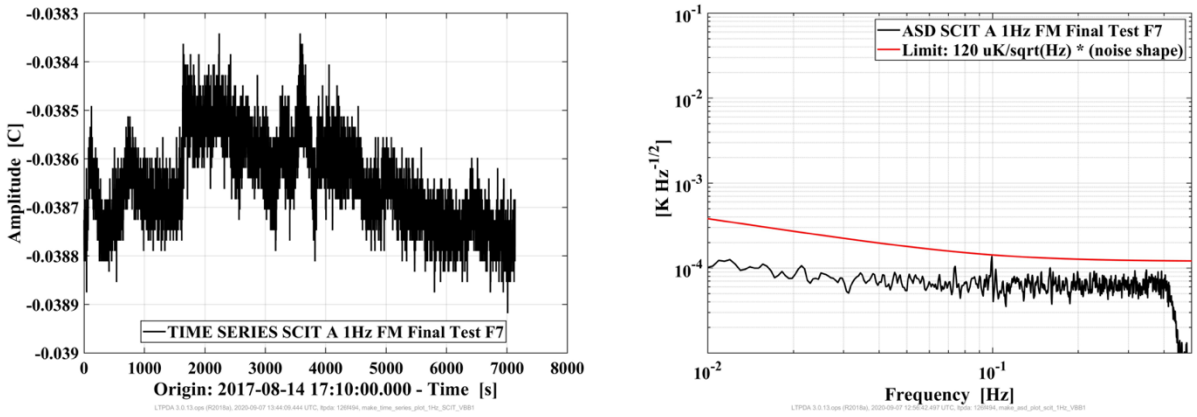

Figure 9 Scientific Temperature (SCIT A) time-series and ASD, measured on a fixed resistor instead of a thermistor. Sampling rate = 1 Hz; 2 h time-series; this measurement has been performed in the final test campaign of E-Box FM before delivery to CNES for SEIS integration.

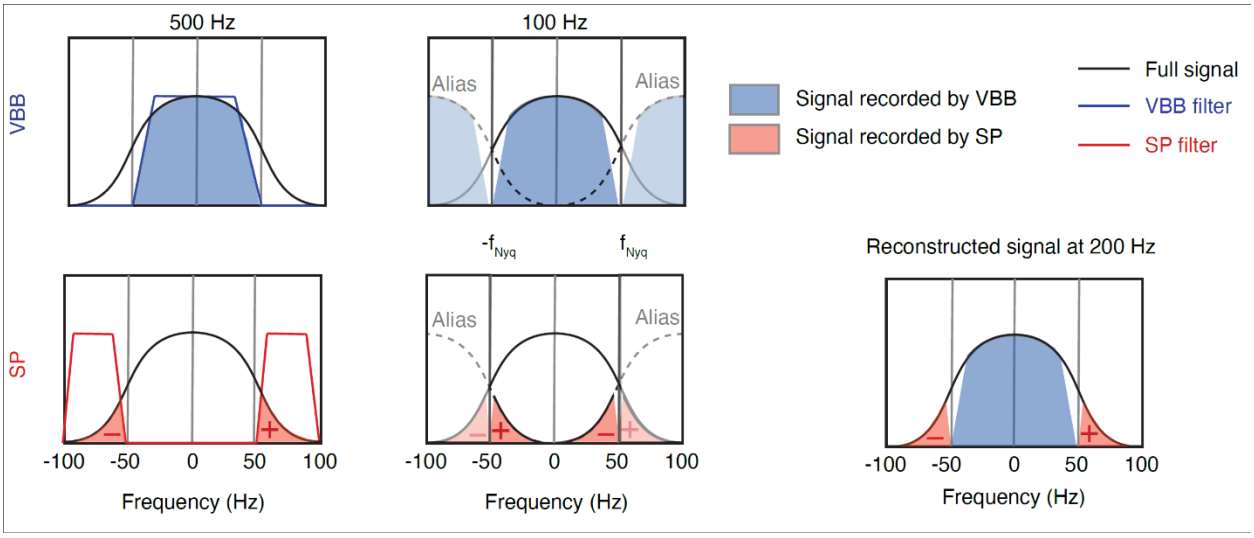

Figure 10 Sampling strategy to record signals with frequencies up to 100 Hz (simulating a sampling rate of 200 Hz from two separate 100 Hz recordings). (Upper row) The VBB data will be acquired with the standard anti-alias filter (0–50 Hz low-pass filter) when down-sampling the signals digitized at 500 Hz to 100 Hz. (Lower row) The SP data will be filtered with a 50–100 Hz band pass filter, which results in the SP data being folded one time. For the reconstruction of the 0–100 Hz bandwidth (corresponding to 200 Hz sampling; see rightmost sketch), the aliased SP data are folded back before adding the VBB and SP data together. Due to the periodicity of the Fourier transform, down-sampling to 100 Hz will cause the signal to be periodically repeated along the frequency axis at a spacing of 100 Hz (so-called aliases). The different filters used for the SP and VBB channels ensure that the aliases do not overlap, so that they can be individually isolated and used for the reconstruction.

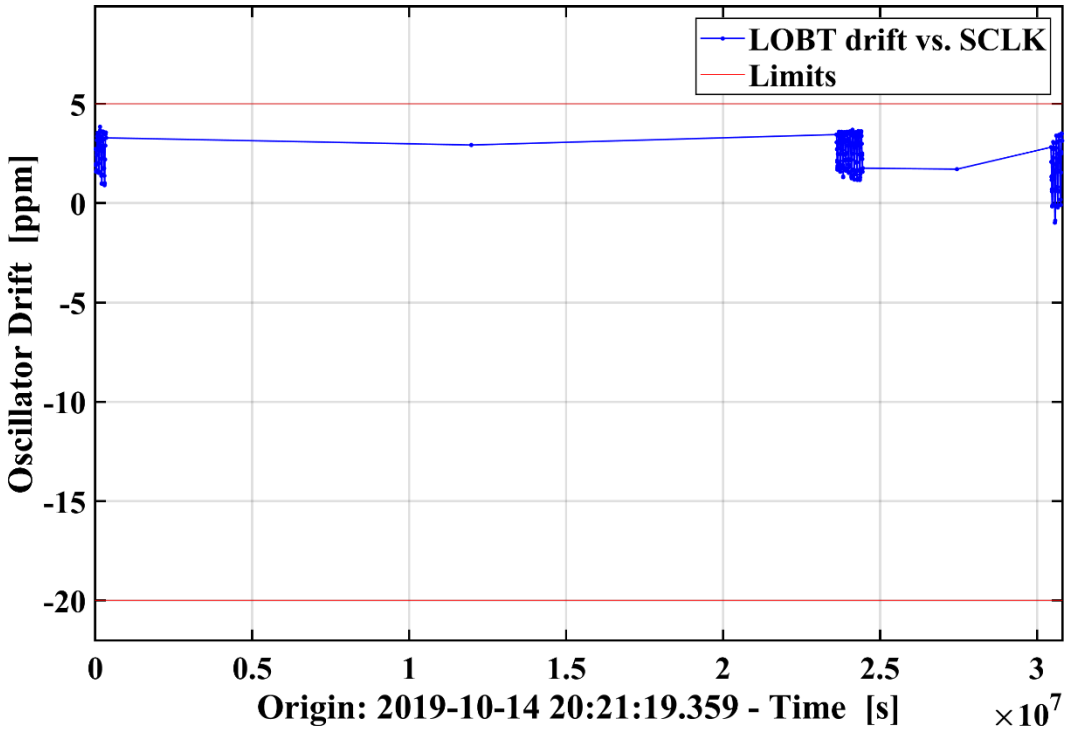

Figure 11 The drift of the LOBT versus the SCLK in the second reporting period from 2019-10-14 to 2020-10-05

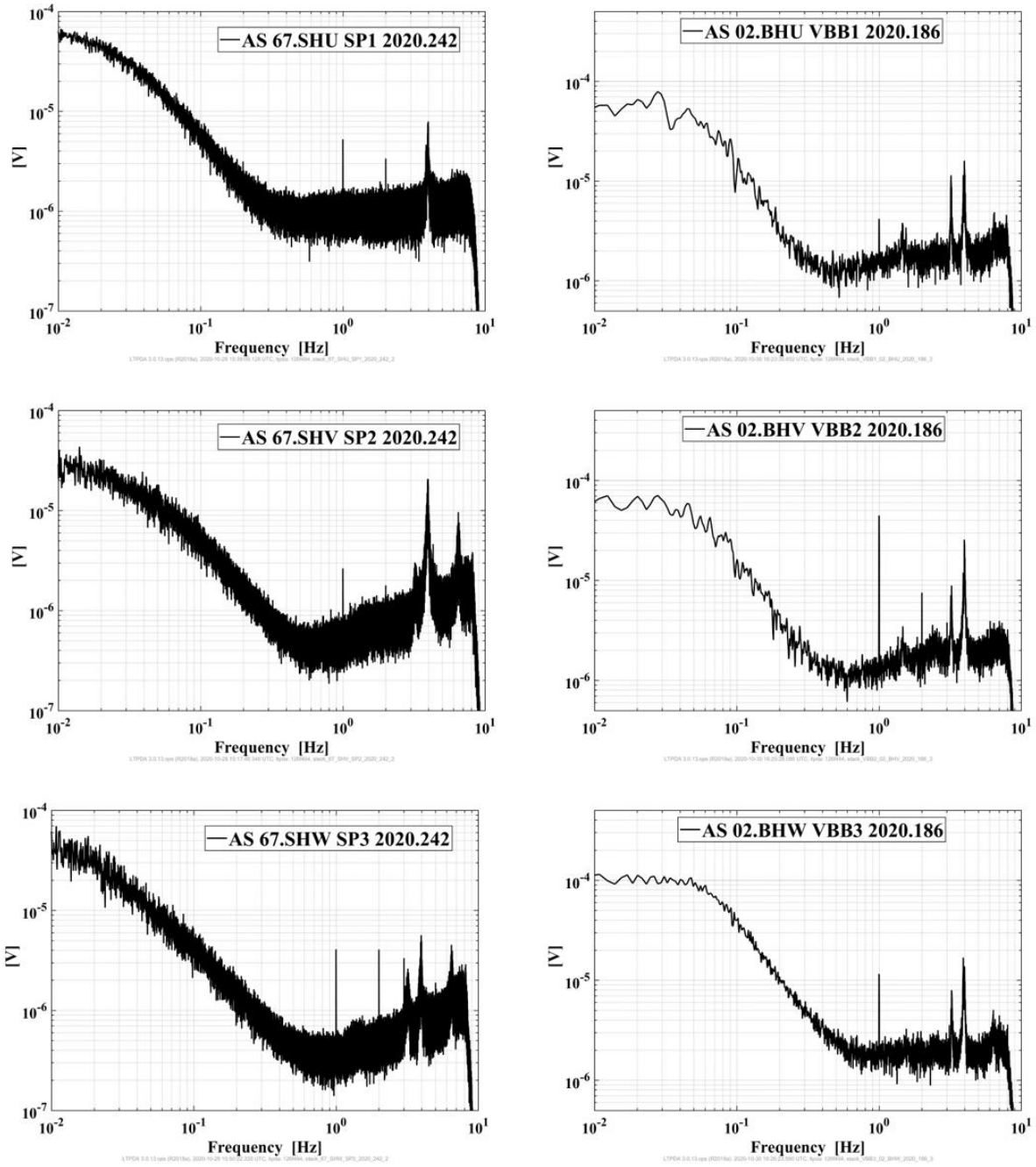

978

979 Figure 12 Left side: Amplitude spectra of SP1, SP2 and SP3 channels at high gain and 20 Hz sampling rate;
980 24 h time-series; start time 2020-08-29 00:00:00 UTC; tick-noise amplitudes calculated from the samples
981 of the stacked signal: SP1= 7.2 µVrms, SP2 = 3.9 µVrms, SP3 = 7.4 µVrms. Right side: Amplitude spectra
982 of VBB1, VBB2 and VBB3 channels in high gain and 20 Hz data rate; 40 min time-series; start time at
983 2020-07-04 14:50:00; tick-noise amplitudes calculated from the samples of the stacked signal: VBB1 =
984 7.5 µVrms, VBB2 = 49.2 µVrms, VBB3 =14.2 µVrms

985

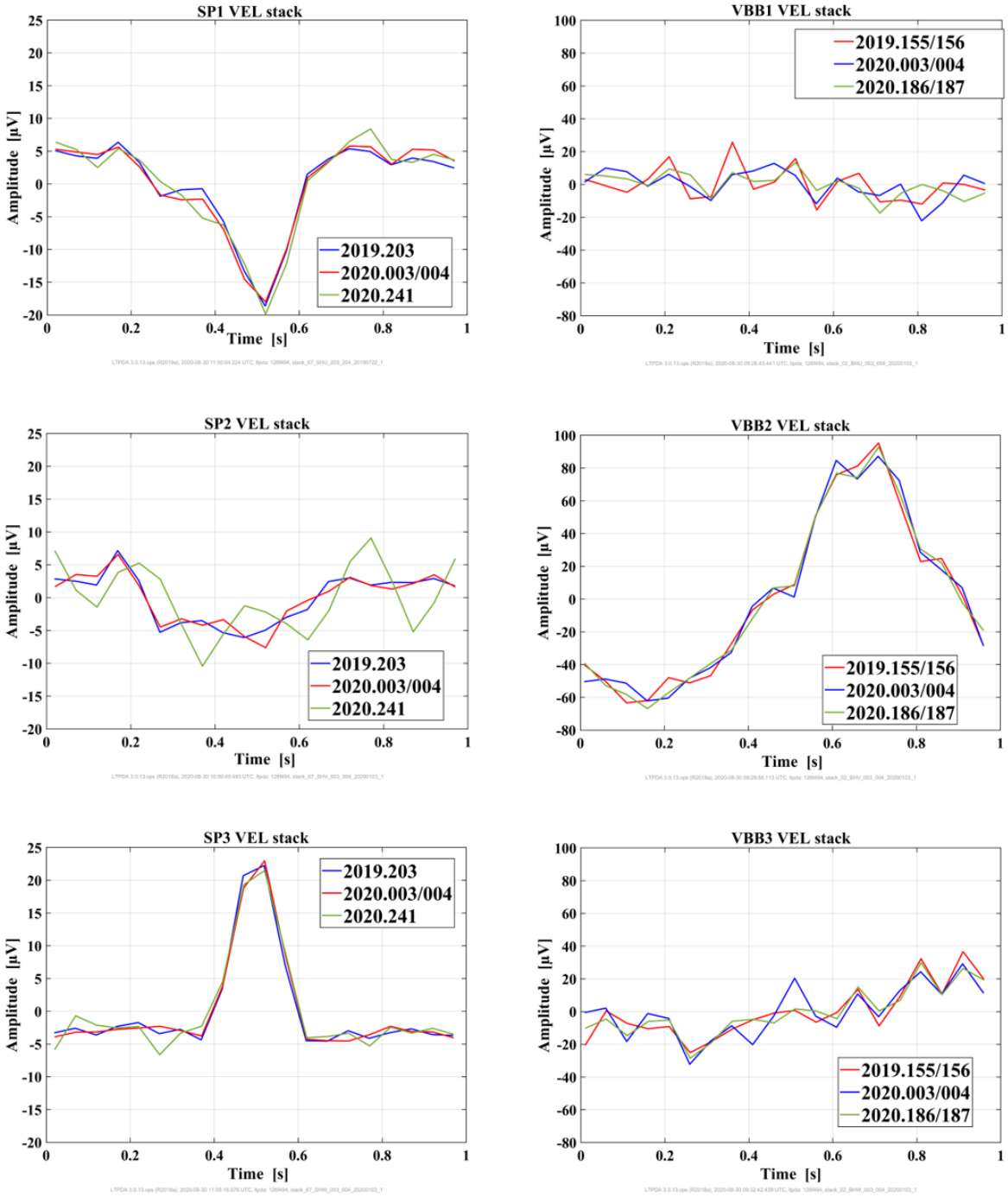

Figure 13 Left side: Stacked waveforms for SP1, SP2 and SP3 at high gain and 20 Hz sampling rate; recordings from 2019-07-22 (18 hours), from 2020-01-03 (48 hours) and from 2020-08-28 (24 hours). Right side: Stacked waveforms for VBB1, VBB2 and VBB3; recordings from 2019-06-04 (48 hours), 2020-01-03 (48 hours) and 2020-07-04 (48 hours)

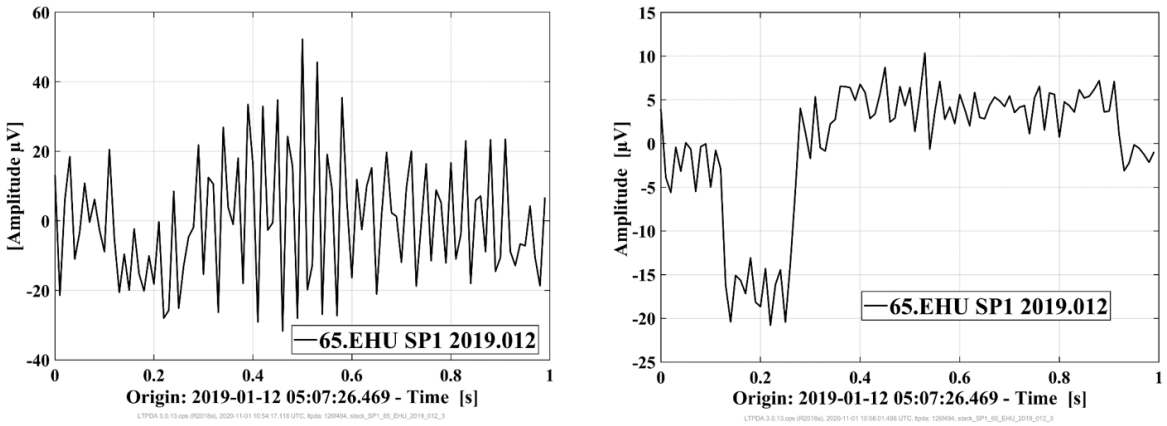

992

993 Figure 14 Comparison of the stacked waveform, SP1, recorded on 2019-01-12 at 05:07:26 for 48 min, with
994 100 Hz sample rate, high-pass filter with 0.1 Hz corner frequency; left: all available data is stacked, right:
995 variance level set to 10^{+4} counts; 328 of 2880 1-second chunks were rejected

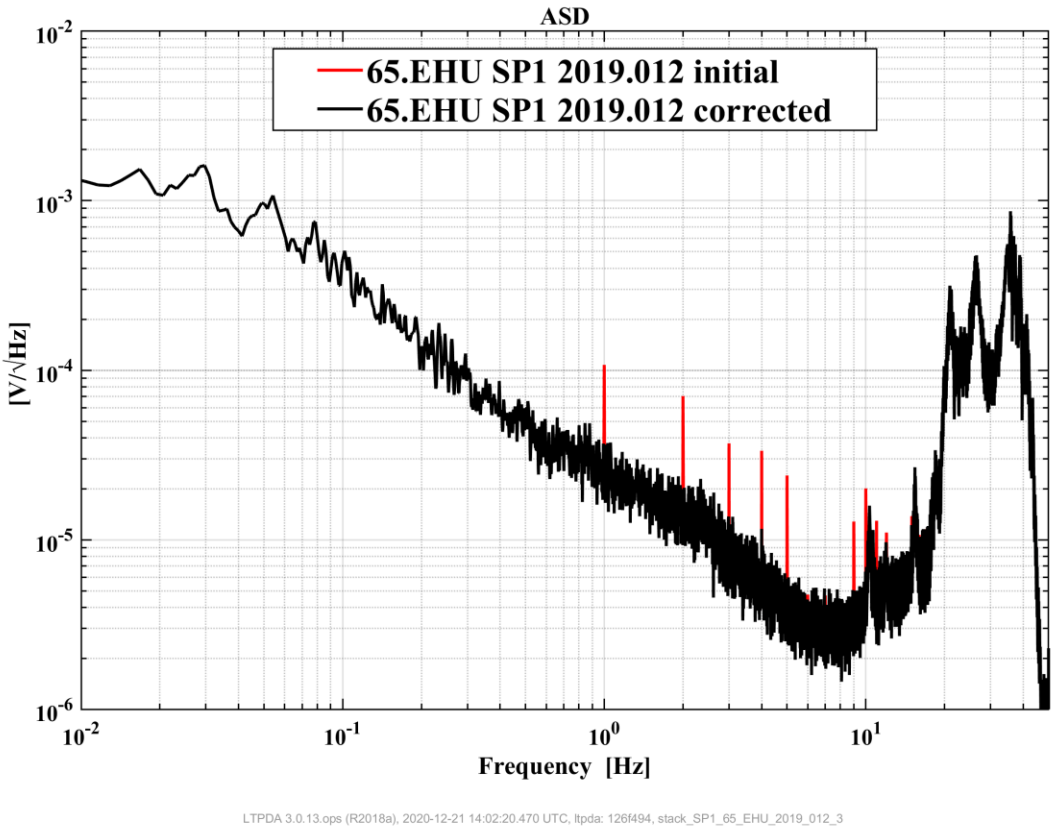

996

997 Figure 15 Corrected SP1 data, high-pass filter with 0.1 Hz corner frequency, accepting waveform chunks
998 for the stacking process only with a variance below variance level 10^{+4} counts, as in Figure 14 on the right
999 side. Data recorded on 2019-01-12 at 05:07:26 for 48 min, with 100 Hz sample rate.

1000

Appendices (optional) – equations, figures and tables labeled using "A" (i.e. Table A1, A2; Figure A1, A2; Eq. A1, A2, etc.)

Electronic Supplement (optional) – Authors may submit supplemental digital material to accompany papers. See Electronic Supplement Guidelines for further instructions. If your paper has an electronic supplement, include citations for this material in the text (i.e. "for a complete list of earthquakes, see Table S4 in the electronic supplement to this article.")

Supplemental Material (All Other Files, i.e. Movie, Zip, tar)

Click here to access/download

Supplemental Material (All Other Files, i.e. Movie, Zip, tar)

PYTHON_tickrem_20210225.zip